TEM for Characterization of Core-Shell Nanomaterials

6

Yiqian Wang and Chao Wang

Contents

1 Definition of the Topic

Transmission electron microscope is an essential tool for characterization of nanoscale materials and devices because it can shed light on the microstructure of nanomaterials. For core-shell nanostructured materials, transmission electron microscopy (TEM) can provide much more important information: overall particle size, core size, shell thickness, uniform or nonuniform shell coating, lattice fringe, elemental distribution, etc. In this chapter we will describe the application of TEM for characterization of core-shell nanomaterials.

Y. Wang (✉) • C. Wang
The Cultivation Base for State Key Laboratory, Qingdao University, Qingdao, People's Republic of China
e-mail: yqwang1013@yahoo.com.cn; yqwang@qdu.edu.cn

C.S.S.R. Kumar (ed.), *Transmission Electron Microscopy Characterization of Nanomaterials*, DOI 10.1007/978-3-642-38934-4_6,

2 Overview

Nanomaterials have, by definition, at least one dimension in the range of 1–100 nm and subsequently show novel properties different from their bulk materials. The synthesis, characterization, and applications of nanomaterials are the most important parts among the wide range of nanotechnology areas falling under the general "nanotechnology" umbrella. In recent years, core-shell nanomaterials have attracted much attention for their excellent physical properties and chemical stability.

However, traditional characterization tools such as scanning electron microscope (SEM) and atomic force microscope (AFM) can only reflect the surface features of core-shell nanomaterials, lacking detailed information from the core. This is due to the fact that the core is embedded in the shell which is made up of complex materials such as metal, silica, and organics.

Here we describe how to employ TEM to investigate the interface between the core and shell, shape of the core and shell, uniform or nonuniform shell coating, formation of core-shell structure, etc.

3 Introduction

Nanostructured materials have drawn significant attention as potential building blocks for nanocomposites, nanoscale electronic devices, ultrahigh-density magnetic recording systems, and optical devices. The most important characteristics, among many others, on a nanoscale are as follows. First, the small size of nanomaterials leads to an increased surface area to volume ratio and as a result the quantum confinement effects dominate. Second, the increasing surface area to volume ratio leads to an increase in the dominance of the surface atoms over those in its interior.

Initially a lot of research work focused on single-phase nanoparticles because such nanomaterials had much better properties than bulk materials. In the late 1980s, it was found that heterogeneous composite or sandwich colloidal semiconductor nanoparticles had better efficiency than their corresponding single-phase particles; in some cases they even demonstrated some new properties [1–3]. More recently during the early 1990s, researchers synthesized concentric multilayered semiconductor nanoparticles with an aim to improving their properties. Hence, the terminology "core-shell" was subsequently adopted [4–6]. Furthermore, there has been a gradual increase in research activities because of tremendous need for more and more advanced materials fueled by modern technology. Simultaneously the advancement of characterization techniques has greatly helped to establish the structures of these different core-shell nanomaterials. A statistical data analysis is presented in Fig. 6.1 to show the increasing trend of published research papers in this area. These were collected in June 2012 from "SciFinder Scholar" using the keyword "core-shell nanoparticles."

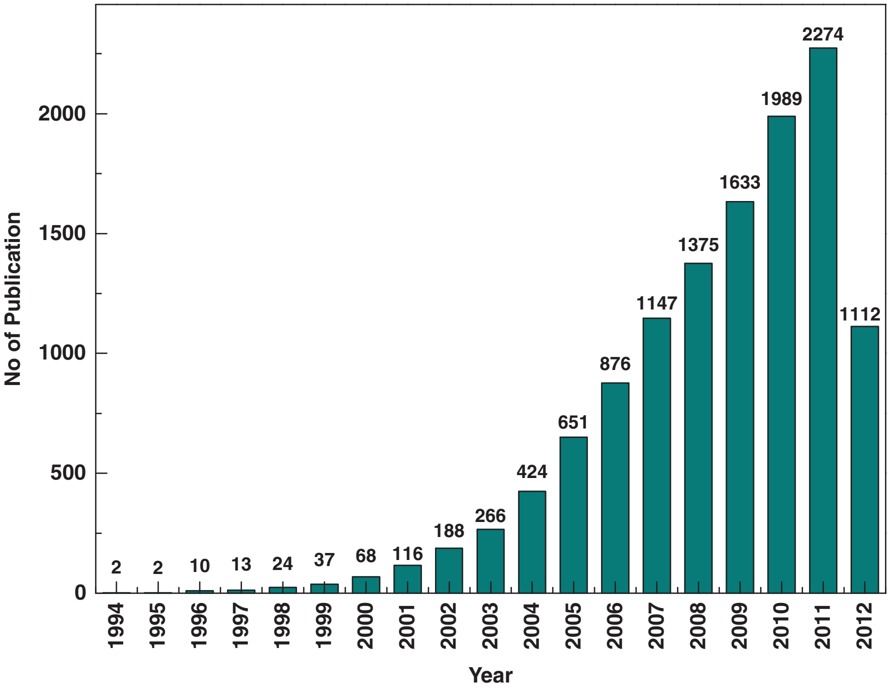

Fig. 6.1 Publications per year for core-shell nanoparticles during the period from 1994 to June 2012 (Data collected from SciFinder Scholar Database)

In recent years, the advances in new synthesis techniques have made it possible to fabricate not only the symmetrical (spherical) nanoparticles but also a variety of other shapes such as cube [7–14], prism [15, 16], hexagon [7, 8, 17–20], octahedron [11, 12], disk [21], wire [22–29], rod [22, 30–37], tube [22, 38–41], etc. Moreover, the structure and composition of core-shell nanomaterials also become more complicated. It means that core-shell nanomaterials are no longer simple spherical particles but are completely coated by a shell of different materials. The shell may have a complex multilayer structure [42–45], and the core may move freely instead of being fixed by the shell [46, 47]. Different classes of core-shell nanoparticles are shown schematically in Fig. 6.2. These core-shell nanomaterials have aroused immense interest because of their novel properties.

Current applications of different core-shell nanoparticles were summarized in a review article by Karele et al. [48] The individual report from different researchers also demonstrated the fact that core-shell nanoparticles are widely used in different applications such as biomedical [49–52] and pharmaceutical applications [53], catalysis [54, 55], electronics [4, 56, 57], enhancing photoluminescence [58–60], creating photonic crystals [61], etc. In particular, in the biomedical field, the majority of these particles were used for bioimaging [51, 62–68], controlled drug release [68, 69], targeted drug delivery [51, 65, 68–70], cell labeling [51, 71], and tissue engineering applications [69, 72].

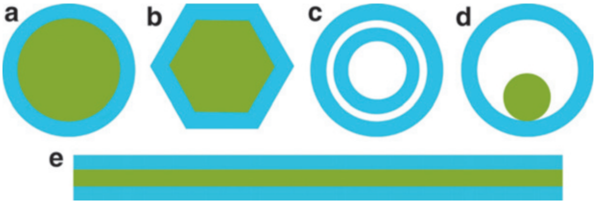

Fig. 6.2 Different kinds of core-shell nanomaterials: (**a**) Spherical core-shell nanoparticles. (**b**) Hexagonal core-shell nanoparticles. (**c**) Double shell core-shell nanoparticles. (**d**) Movable core with hollow shell nanoparticles. (**e**) Core-shell nanowires

Unfortunately, traditional characterization techniques are not good enough to demonstrate the growing complexity of core-shell nanomaterials. However, TEM is an effective method [73] to unlock the secret of the core due to its unique imaging procedure and various techniques.

At present, lots of books have focused on TEM techniques or applications, but few on TEM characterization of core-shell nanomaterials. This chapter is designed to illustrate some TEM techniques for characterizing the core-shell nanostructures, such as diffraction contrast imaging, high-resolution TEM (HRETM), high-angle annular dark-field (HAADF), and elemental mapping. We will take the TEM techniques as a clue to discuss the application of TEM for characterization of core-shell nanomaterials. The characteristic of each TEM technique will be explained and some up-to-date research work will be demonstrated.

4 Experimental and Instrumental Methodology

4.1 Synthesis of Core-Shell Nanomaterials

Approaches for the synthesis of nanomaterials can be broadly divided into two categories: “top-down” and “bottom-up.” The “top-down” approach often adopts traditional workshop or microfabrication methods where externally controlled tools are used to cut, mill, and design materials into the desired shape and order. For example, the most common techniques are lithography techniques [74, 75], laser-beam processing [76], and mechanical techniques [77–79]. “Bottom-up” approach, on the other hand, exploits the chemical properties of the molecules to let them self-assemble into some useful conformations. The most common bottom-up approaches are chemical synthesis, chemical vapor deposition, laser-induced assembly, self-assembly, colloidal aggregation, film deposition and growth [80–82], etc. Currently it is hard to say which approach is superior because each has its advantages and disadvantages. However, the bottom-up approach can produce much smaller particles and has the potential to be more cost-effective in the future due to the advantages of absolute precision, complete control over the process, and minimum energy loss compared with that of a top-down approach. As far as the synthesis of core-shell nanomaterials is concerned, the bottom-up approach has proven to be more suitable since the ultimate control is required for achieving a uniform coating of the shell materials during the particle formation. A combination of these two approaches can also be utilized. For example, core particles can be synthesized by a top-down approach and then coated by a shell fabricated by a bottom-up approach which could maintain uniform and precise shell thickness. To control the overall size and shell thickness precisely, a microemulsion instead of a bulk medium is preferable because water droplets can act as a nanoreactor template.

4.2 Transmission Electron Microscopy Techniques

TEM is a characterization technique whereby a beam of electrons transmits through an ultrathin specimen and interacts with the atoms or molecules in the specimen [73]. TEM is capable of imaging at a significantly higher resolution than light microscopes, owing to the small de Broglie wavelength of electrons. TEM has various imaging techniques, such as diffraction contrast imaging, high-resolution TEM, high-angle annular dark-field, and elemental mapping.

TEM bright field (BF) image is mainly caused by amplitude contrast. Amplitude contrast results from variations in mass or thickness or a combination of the two: the thickness variation can produce contrast because the electron interacts with more material (hence, more mass). Alternatively, diffraction can vary locally because the specimen is not a perfect, uniformly thin sheet. In order to translate the electron scatter into interpretable amplitude contrast, we use objective aperture which is placed in the back focal plane of the objective lens to select the direct beam in the selected area electron diffraction (SAED) to form BF images. Regions of no specimen show a bright background, and regions of the specimen that are thick or dense will present dark in the image.

The HAADF image is also called Z-contrast image. The HAADF image contrast is usually proportional to the Z^2 (Z is atomic number). Because of Bragg scattering, normal ADF detector is not suited for the study of crystalline specimens. But we can decrease the camera length with the post-specimen lenses to ensure that the Bragg electrons (including any HOLZ scattering) do not hit the detector. Thus, only the electrons scattered through very high angles contribute to the image. Bragg scattering effects are avoided if the HAADF detector only gathers electrons scattered through an angle larger than 50 mrad ($\sim 3°$).

HRTEM is an important imaging technique in TEM, from which we can obtain the atomic structure information from a specimen. HRTEM image is mainly caused by phase contrast, and it is produced by interference of the transmitted beam with at least one diffracted beam. When performing HRTEM experiments, we should select a larger objective aperture and let through more beams carrying with their amplitudes and phases to produce a phase contrast image.

Elemental mapping is one important technique in energy-filtering transmission electron microscopy. Elemental maps extracted from ionization edges can obviously show the spatial distribution of elements in samples. Usually two methods, two-window and three-window, are used to get this information. Two-window method is acquiring two images from electrons in selected energy windows, a pre-edge background image and a post-edge image, and then obtaining the ratio images of pre- and post-edge windows, which can give a qualitative elemental distribution. Three-window method is acquiring three images from electrons in selected energy windows: two pre-edge windows used to calculate the background fit and one post-edge window in which the extrapolated background is subtracted from the total intensity to leave the edge intensity. This method can give quantitative images of the distribution of specific elements.

Alternative operation modes of use allow for TEM to observe modulations in chemical composition, crystal orientation, and electronic structure.

5 Key Research Findings

5.1 Application of Diffraction Contrast Imaging in Nanomaterials

TEM image contrast arises because of the scattering of the incident beam by the specimen. For core-shell structure materials, the components of core and shell are different. As a result, it will produce a strong contrast in the BF image. Through the BF image, we can determine the formation of core-shell structure and measure the thickness of core and shell. In this section, we will discuss the application of TEM BF image for characterization of core-shell nanomaterials in detail.

5.1.1 Silica-Coated Core-Shell Nanomaterials

The silica coating has several advantages. The most basic advantages of the silica coating compared with other inorganic (metal or metal oxide) or organic coatings are as follows: It reduces the bulk conductivity and increases the suspension stability of the core particles. In addition, silica is the most chemically inert material available, and it can block the core surface without interfering the redox reaction at the core surface. Silica coatings can also be used to modulate the position and intensity of the surface plasmon absorbance band since silica is optically transparent. As a result, chemical reactions at the core surface can be studied spectroscopically. Therefore, researchers are more interested in the silica coatings on different inorganic core materials such as metals [83–94], binary inorganic composites [95–97], metal oxides [98–101], and metal salts [88, 102–106] than any other combination.

According to the literature, the shell thickness from 8 to 100 nm can be controlled by adjusting the experimental parameters such as coating time, concentration of reactants, catalyst, and other precursors [83, 84, 87]. Figure 6.3 shows Au@SiO_2 nanoparticles where the shells have different thicknesses [107]. These nanoparticles were prepared in the following steps. Gold colloids were homogeneously coated with silica using the silane coupling agent (3-aminopropyl)-trimethoxysilane as a primer to render the gold surface vitreophilic. After the formation of a thin silica layer in aqueous solution, the particles were transferred

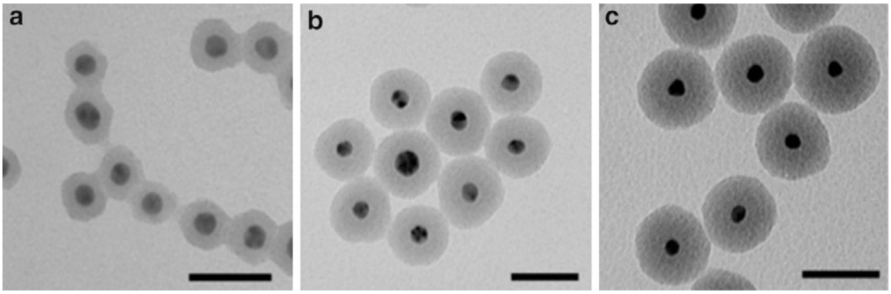

Fig. 6.3 TEM images of Au@SiO_2 nanoparticles. The core dimension is ~15 nm and the silica shells are around 8, 18, and 28 nm, respectively. Scale bars are 50 nm in all images [107] (Reprinted with permission from ref 107. Copyright 2002 Wiley-VCH)

into ethanol for further growth using the Stöber method [108]. From the BF image, we can find that the core is darker compared with the shell, mainly because the gold core has a stronger scattering ability than the silica shell. The image contrast is so clear that we can easily measure the size of core and shell through the image. The gold core is ~15 nm in diameter and a silica shell thickness ranges from 8 to 28 nm.

$CoFe_2O_4$ receives much attention in the biomedical field for its high magnetic anisotropy and saturation magnetization which give rise to suitable magnetic behavior at room temperature, but the presence of cobalt makes it potentially toxic [109, 110]. To protect magnetic nanoparticles, encapsulation both in polymeric and inorganic matrices has been proposed [111], while silica has been most often used [112]. Spherical nanoparticles of surfactant-coated $CoFe_2O_4$ (core) were prepared through thermal decomposition of metal acetylacetonates in the presence of a mixture of oleic acid and oleylamine and uniformly coated with silica shell by using tetraethyl orthosilicate and ammonia in a micellar solution (core/shell) [113]. TEM analysis of core-shell nanoparticles evidenced the high homogeneity of the coating process in producing single core-shell nanoparticle with a narrow size distribution. TEM images (Fig. 6.4a, b) in BF mode show the formation of spherical core-shell structures with an average overall size of 30 nm and a polydispersity of 5 % (Fig. 6.4c) with a single magnetic core in the center of the sphere. TEM image in dark-field mode (Fig. 6.4d) confirms the high degree of crystallinity of the core and the amorphous nature of the shell. The assembling of the nanoparticles appears to be in the form of hexagonal close packing. In some cases a deviation from spherical shape can be observed (Fig. 6.4b); this can be caused by a slight deformation of the particles along the close packing direction.

In some cases the density/concentration of one shell is different. Since the shells with different density/concentration own different scattering ability which will show different TEM image contrast, TEM BF imaging technique is also applied to characterize such kind of materials. Ge et al. [42] prepared nanoparticles in a facile and scalable way, and the procedure was outlined in Fig. 6.5. A monolayer of the metal nanocatalyst was first immobilized on the surface of silica colloids by using coupling agents. The core-satellite structures were then coated with another

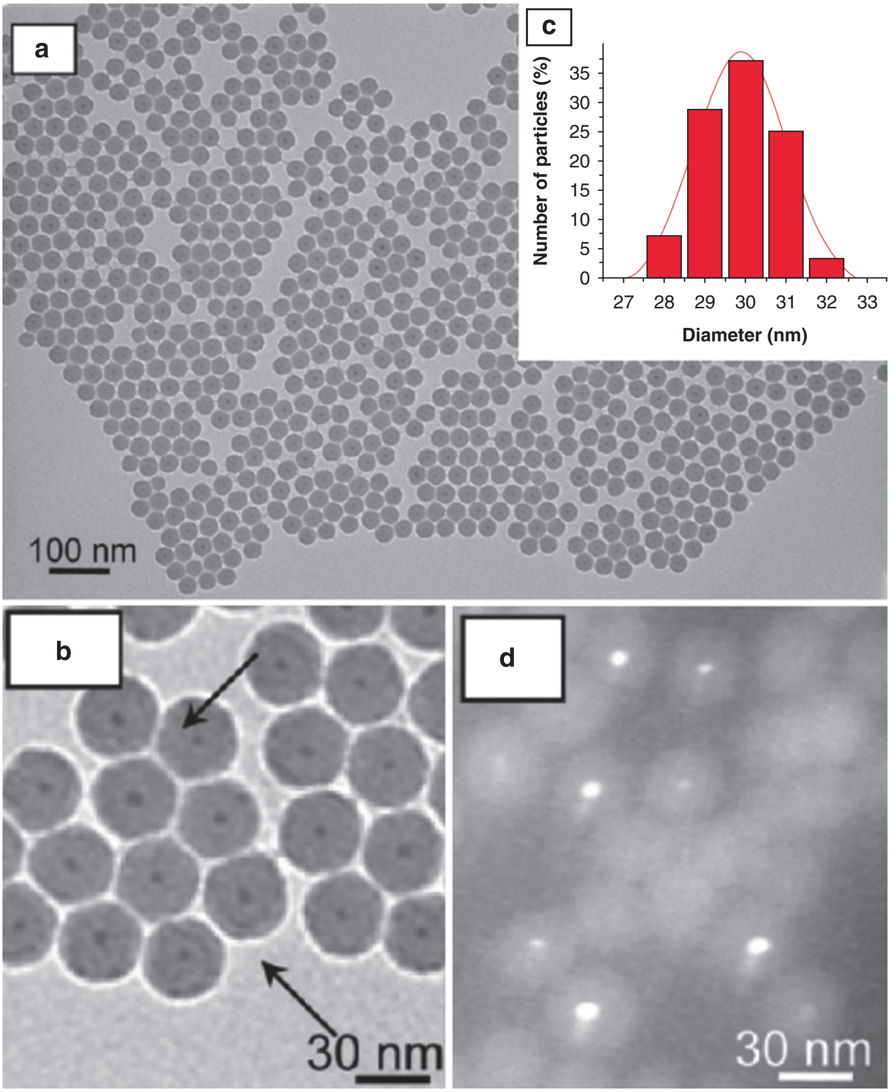

Fig. 6.4 TEM data of $CoFe_2O_4$-SiO_2 core-shell nanoparticles. (**a**) BF image at low magnification. (**b**) BF image at high magnification. (**c**) Particle size distribution. (**d**) Dark-field image [113] (Reprinted with permission from Ref. [113]. Copyright 2010 American Chemical Society)

layer of silica of the desired thickness to fix the position of metal nanoparticles. Finally, a "surface-protected etching" technique was applied to make the outer shell mesoporous, exposing the catalyst particles to outside chemical species [114]. To improve the recyclability, they also incorporated a superparamagnetic Fe_3O_4 core at the center of the initial silica colloids [115, 116]. The etching process can be well controlled by monitoring the transmittance of the colloidal solution. With an

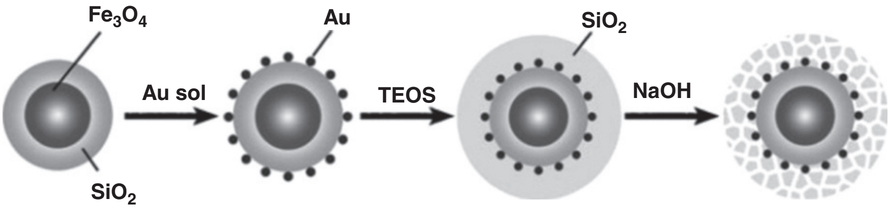

Fig. 6.5 Synthetic procedure of porous silica protected $Fe_3O_4/SiO_2/Au$ composite structures [42] (Reprinted with permission from Ref. [42]. Copyright 2008 Wiley-VCH)

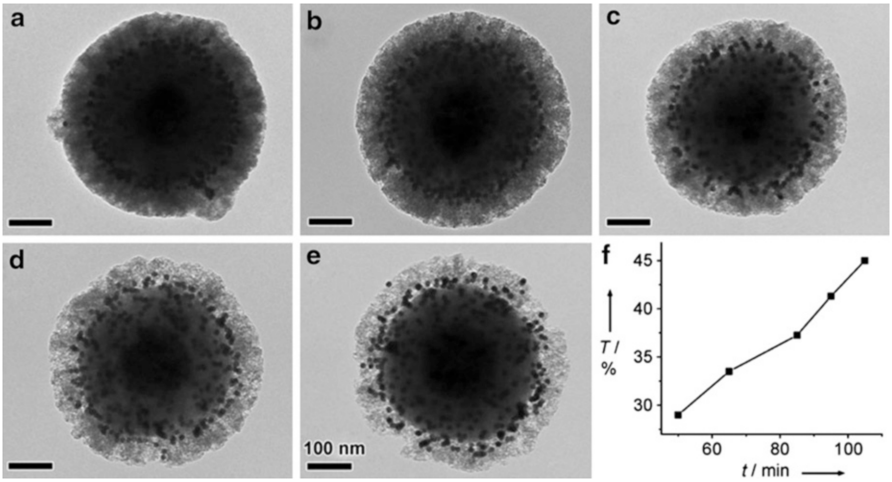

Fig. 6.6 (**a**–**e**) TEM BF images of $Fe_3O_4/SiO_2/Au/por\text{-}SiO_2$ composite colloids collected after different etching times: (**a**) 50, (**b**) 65, (**c**) 85, (**d**) 95, and (**e**) 105 min. (**f**) Changes in transmission intensity of the solution ($\lambda = 1{,}000$ nm) with etching time [42] (Reprinted with permission from Ref. [42]. Copyright 2008 Wiley-VCH)

increase of etching time, more silica materials dissolved in the form of soluble silicate oligomers, and accordingly the transmittance increased. Figure 6.6 shows typical TEM BF images of five $Fe_3O_4/SiO_2/Au/por\text{-}SiO_2$ composite colloids collected after 50, 65, 85, 95, and 105 min of etching [42]. It is clear that the thickness of shell shows no apparent change as time goes on, but the contrast between core and shell tends to be sharp. This is due to the fact that the shell is composed of a porous structure which has a weak scattering ability. Consistently, the transmittance of the solution increases from 29 % to 45 % with a near-linear dependence on the reaction time (Fig. 6.6f).

As an alloying electrode material, Si has attracted much attention because of its highest known theoretical charge capacity. One interesting behavior for an amorphous Si (a-Si) is that it reacts with lithium (Li) at slightly higher potential (~220 mV) [117, 118] than crystalline Si (c-Si) does (~120 mV) [119, 120], which leads to an idea of using c-a core-shell Si nanowires (NWs) as an anode material. When limiting the charging potential, it should be possible to utilize only the amorphous shell material for Li storage while preserving the crystalline core as mechanical support and efficient electron transport pathways, as indicated in Fig. 6.7a. Figure 6.7 shows c-a core-shell Si NWs grown directly on stainless steel (SS) current collectors by a simple one-step synthesis. Cui et al. [121] found that large flow, high pressure, and high temperature promote the yield of c-a core-shell Si NWs on SS substrates. As shown in Fig. 6.7b, the thickness of amorphous shell increases linearly with growth time, while the core radius does not change. This suggests that c-Si cores grew first and a-Si was subsequently coated onto the cores from SiH_4 decomposition. Figure 6.7c–h shows the TEM images, selected SAED patterns, and HRTEM images of Si NWs grown at 485 °C for different growth times. After 10 min of growth, the NWs were mostly single crystalline (Fig. 6.7c, d) with little amorphous shell. After 20 min, a thick layer of amorphous shell was observed (Fig. 6.7e, f), which became even thicker after 40 min (Fig. 6.7g, h). Consistently, the SAED pattern in Fig. 6.7g shows amorphous diffraction ring which is not found in Fig. 6.7c.

5.1.2 Bimetallic Core-Shell Nanomaterials

Bimetallic core-shell and alloy nanoparticles have received intense attention, owing to their novel optical, electronic, magnetic, and catalytic properties different from those of individual metals [122–124]. Since these properties strongly depend on composition, shape, and size of the nanoparticles, extensive studies have been focused on the controlled synthesis of these nanoparticles with specific compositions and morphologies [125–140]. For the bimetallic core-shell nanostructures, a direct approach to determine their structure is TEM because a clear boundary between core and shell can be distinguished by bright or dark contrast in the TEM BF image. HAADF and HRTEM techniques can also be employed to characterize bimetallic core-shell structure. We will introduce them in detail in the following section.

Tsuji et al. [141, 142] synthesized shape-dependent Au@Ag core-shell nanocrystals successfully by using a two-step method. In order to understand growth mechanisms of these Au@Ag core-shell particles, they added Au seeds with different shapes into $AgNO_3$/DMF solution at $[AgNO_3]/[HAuCl_4]$ molar ratios of 1, 9, and 18, respectively. From the TEM BF images (Fig. 6.8), we can observe a mixture of Au@Ag core-shell nanocrystals with various shapes. Obviously, truncated-triangular and hexagonal plate-like Ag shells overgrew from triangular and hexagonal Au cores, respectively, whereas decahedral and octahedral Ag shells overgrew from the decahedral and octahedral Au cores, respectively. In addition, it can be clearly seen that the thickness of shell increased over $[AgNO_3]/[HAuCl_4]$ molar ratio. At low $[AgNO_3]/[HAuCl_4]$ molar ratio of 1, thin triangular and hexagonal shells are epitaxially formed over the triangular and hexagonal Au plate cores (Fig. 6.8a, b). With an increase of the $[AgNO_3]/[HAuCl_4]$ molar ratio, larger triangular, truncated-triangular, or hexagonal Ag shells are overgrown. The edge length of Ag shells enlarges with an increase of the molar ratio for the

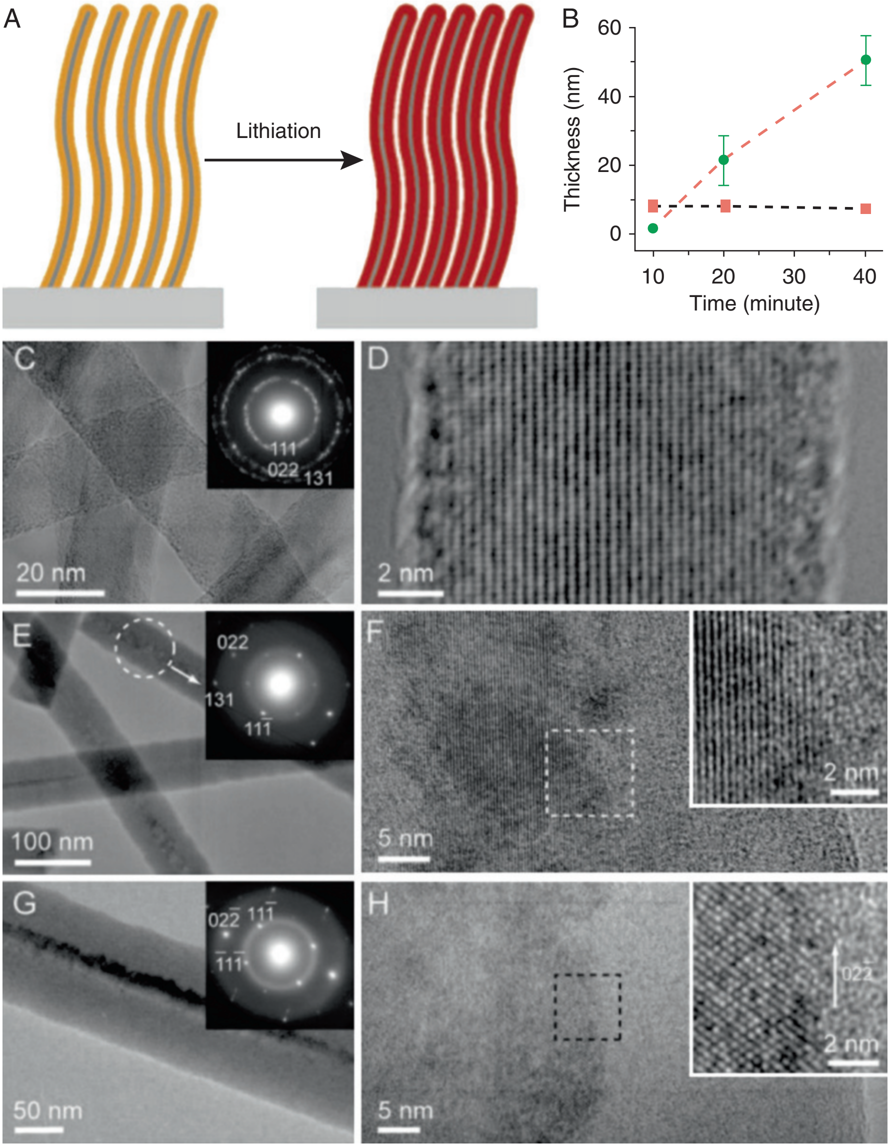

Fig. 6.7 (**a**) Schematic illustration of the lithiation of the c-a Si core-shell NWs grown on a stainless steel substrate. (**b**) Statistics of the core radius (*red*) and shell thickness (*green*) versus growth time. The growth temperature was 485 °C. (**c**) TEM and SAED images of NWs grown for 10 min. (**d**) HRTEM image of a nanowire grown for 10 min. (**e**) TEM and SAED images of NWs grown for 20 min. (**f**) HRTEM images of a nanowire grown for 20 min. (**g**) TEM and SAED images a nanowire grown for 40 min. (**h**) HRTEM images of a nanowire grown for 40 min [121] (Reprinted with permission from Ref. [121]. Copyright 2009 American Chemical Society)

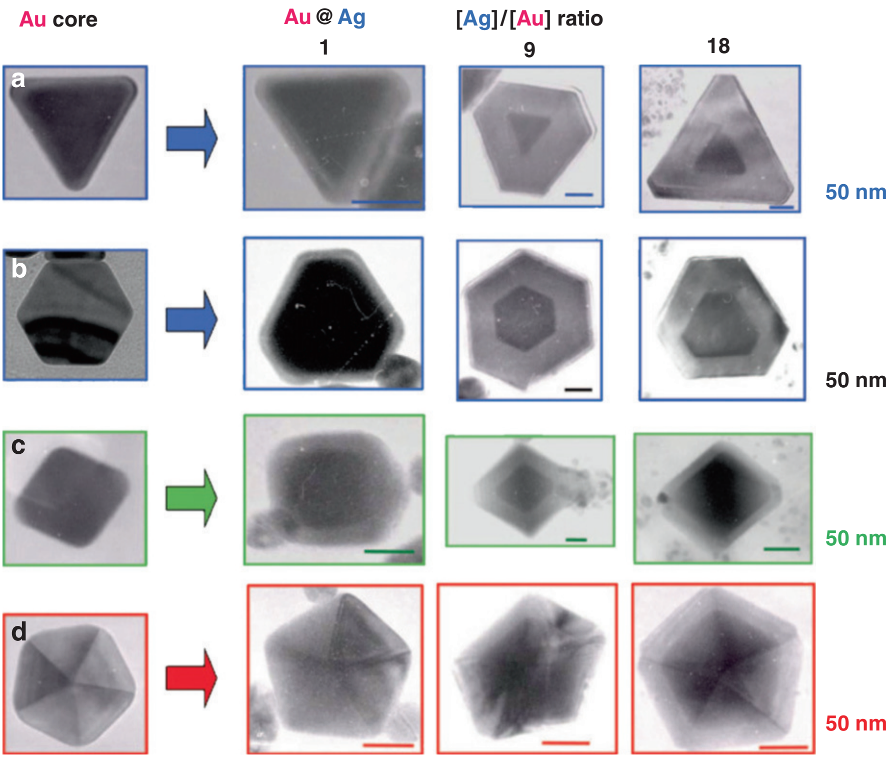

Fig. 6.8 TEM BF images of the Au cores synthesized by a microwave heating for 3 min and the Au@Ag nanocrystals prepared at different [$AgNO_3$]/[H_2AuCl_4] molar ratios by an oil-bath heating [142] (Reprinted with permission from Ref. [142]. Copyright 2008 American Chemical Society)

[$AgNO_3$]/[$HAuCl_4$]. At the highest [$AgNO_3$]/[$HAuCl_4$] molar ratio of 18, Ag shell edges can achieve about three times longer than those of plate-like Au cores, but Au cores are still observed easily in a constant contrast. This indicates that the Au@Ag core-shell particles have a plate-like shape. In order to further confirm the crystal structure of triangular and hexagonal particles, TEM imaging has been carried out from different view angles within ±16° (Fig. 6.9). No significant change can be found in the bright and dark contrast of these triangular and hexagonal particles.

5.1.3 Hollow Core-Shell Nanomaterials

As a unique class of structured materials, hollow colloidal particles have attracted growing research efforts owing to their technological importance in a wide range of applications [53, 143–148]. Templating against colloidal particles is probably the most effective and general method for preparation of hollow particles, especially for studies in which a narrow size distribution is required, i.e., self-assembly of photonic crystals. Monodisperse latex and silica spheres are commonly used as

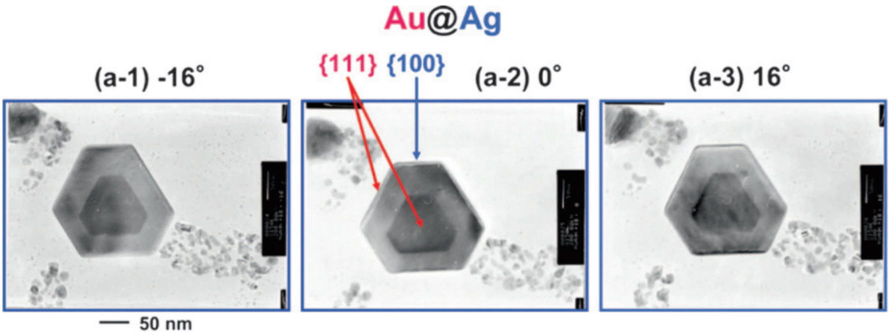

Fig. 6.9 TEM BF images of hexagonal Au@Ag nanocrystal observed from different view angles [142] (Reprinted with permission from Ref. [142]. Copyright 2009 American Chemical Society)

colloidal templates because they are readily available in a wide range of sizes [149–156]. In this section we will introduce some kinds of hollow core-shell nanomaterials which are characterized by TEM.

Figure 6.10 shows hollow core-shell nanoparticles which were designed for a double-electrode nanomaterial composed of a V_2O_5 matrix containing a low weight ratio of SnO_2 nanocrystals (10 % or 15 %) [45]. In this nanostructured composite electrode material, SnO_2 nanocrystals are homogenously distributed in a double-shelled V_2O_5 hollow nanocapsule. The V_2O_5-SnO_2 double-shelled nanocapsules were synthesized by a solvothermal treatment and final heat treatment in air. The SEM image (Fig. 6.10a) of the V_2O_5-SnO_2 nanocapsules indicates that these nanocomposites can be produced in large scale with an average diameter of 550 nm without aggregation. The inset of Fig. 6.10a shows a schematic structure of one individual double-shelled nanocomposite capsule. The red spheres represent SnO_2 nanocrystals, and the green double shells represent the V_2O_5 matrix. The microstructure and components of these nanocapsules were further studied by means of TEM and SAED. Figure 6.10b shows a TEM BF image of double-shelled V_2O_5-SnO_2 nanocapsules consisting of nanocrystals. A typical double-shelled nanocapsule is shown in Fig. 6.10c, which clearly confirms that these hollow nanocapsules have two thin shells. The diameter of the inner hollow nanocapsules is about 430 nm, and the inner cavity is around 250 nm. The thickness of the inner and outer walls can be determined to be ~90 nm through TEM BF image in Fig. 6.10d. To investigate the distribution of SnO_2 in the shell, HRTEM characterization was carried out. The micrographs in Fig. 6.10e and g are HRTEM images taken from the wall edge of the nanocapsules shown in Fig. 6.10d at different locations. Figure 6.10e shows a HRTEM image of a single nanocrystal that reveals the (310) lattice planes of V_2O_5. Figure 6.9f and g reveals the (110) and (101) lattice planes of SnO_2, respectively. These HRTEM images confirm that SnO_2 nanocrystals are homogeneously distributed in the V_2O_5 matrix (double shell). The polycrystalline nature of these nanocapsules was also confirmed by the SAED measurements (Fig. 6.10h). The formation mechanism of the

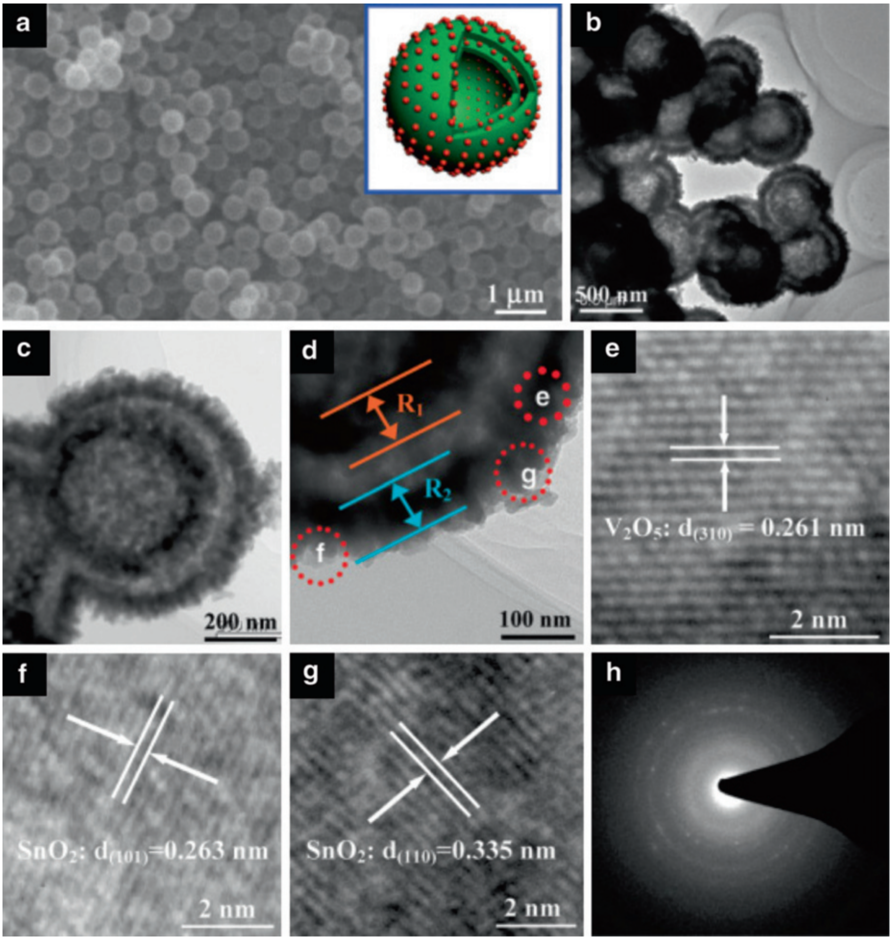

Fig. 6.10 (**a**) SEM image of V_2O_5-SnO_2 double-shelled nanocapsules. The *inset* shows a schematic structure of a double-shelled nanocapsule. The *red* spheres represent SnO_2 nanocrystals, and the *green* double shells represent the V_2O_5 matrix. (**b**) Low-magnification TEM image. (**c**, **d**) High-magnification TEM images showing that the porous shells consist of a great deal of nanocrystals and have thicknesses of R1 $\approx$ R2 90 nm. (**e**, **g**) HRTEM images revealing lattice planes of the V_2O_5 matrix and SnO_2 nanocrystals. (**h**) SAED pattern taken from individual nanocapsules, which shows that these nanocapsules are polycrystalline [45] (Reprinted with permission from Ref. [45]. Copyright 2009 American Chemical Society)

double-shelled hollow nanocapsules is a combination of two types of Ostwald ripening processes (both inward and outward ripening cases).

In order to understand the growth mechanism of double-shelled V_2O_5-SnO_2 hollow nanocapsules, Liu et al. [45] investigated the morphology evolution of the intermediates involved in the formation process. Two intermediates obtained at 5 and 10 h are shown in Fig. 6.11. With a short reaction time (5 h, Fig. 6.11a), the

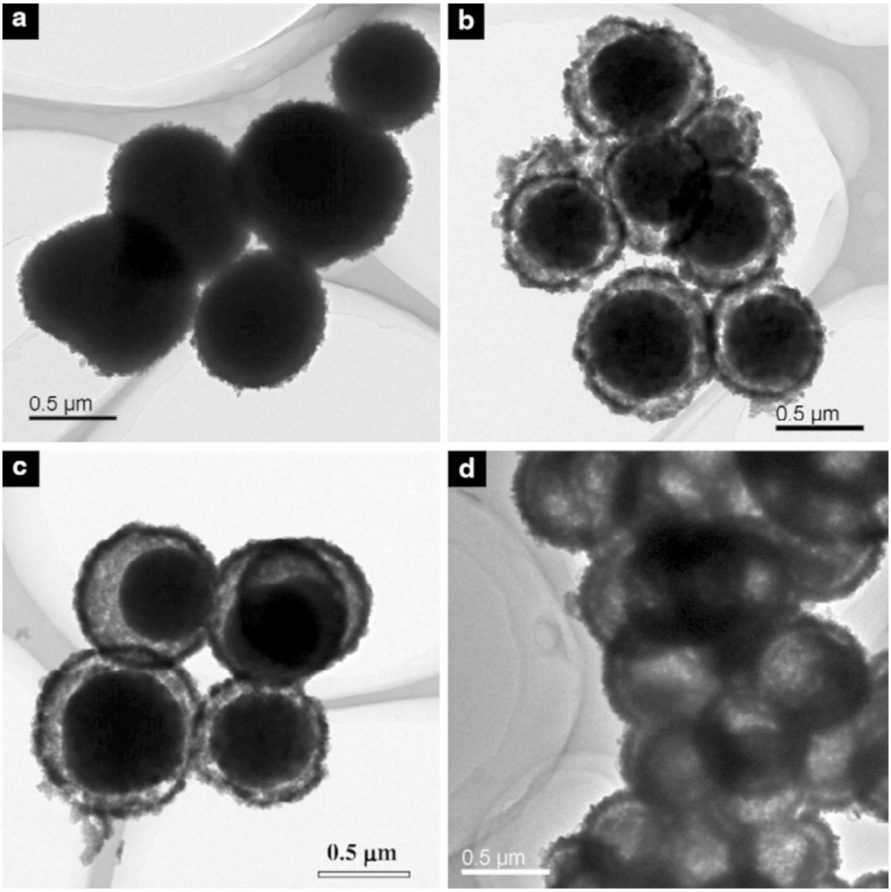

Fig. 6.11 TEM images show the formation process of V_2O_3-SnO_2 composite as double-shelled hollow nanocapsules. (**a**) 5 h, solid V_2O_3-SnO_2 composite nanospheres. (**b**, **c**) 10 h, core-shell intermediates. (**d**) 24 h, double-shelled V_2O_3-SnO_2 hollow nanocapsules [45] (Reprinted with permission from Ref. [45]. Copyright 2009 American Chemical Society)

crystallite aggregates gave a spherical morphology. When the reaction time was extended to 10 h, these solid spheres were converted into solid core-shell particles (Fig. 6.11b, c), and finally this solid core became hollow to form double-shelled hollow nanocapsules (Fig. 6.11d). They concluded that the formation mechanism of the double-shelled hollow nanocapsules is a combination of two types of Ostwald ripening processes (both inward and outward ripening cases). Ostwald ripening firstly took place at the surface of solid spheres, which differed from the previous simpler outward ripening process. Following this inward ripening process, the solid core of core-shell spheres ripened outward furthermore, and finally the double-shelled nanocapsules were achieved.

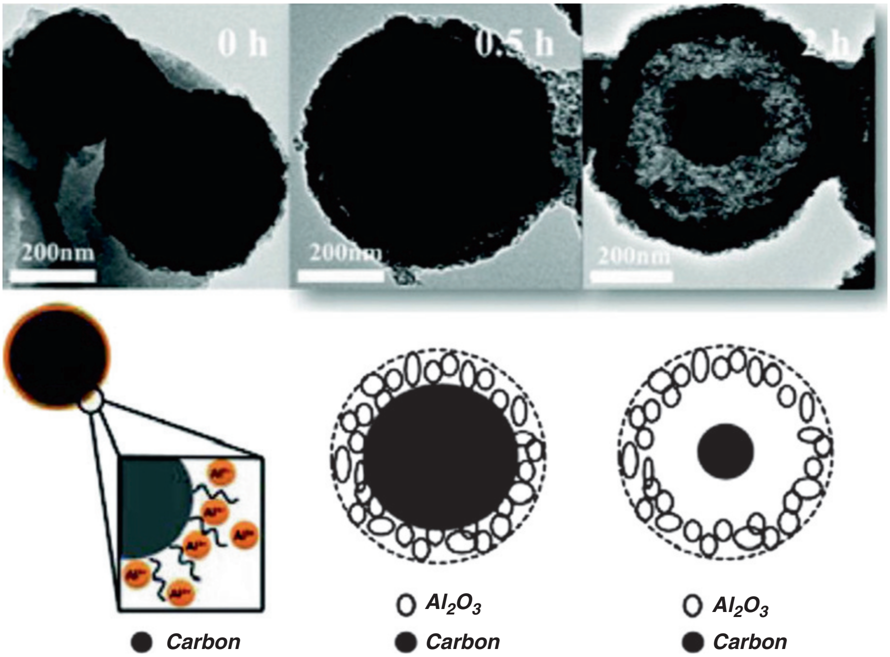

Fig. 6.12 Schematic illustration of the formation of rattle-type carbon-alumina particles; TEM images represent the samples obtained by calcination at 450 °C for 0, 0.5, and 2 h, respectively [159] (Reprinted with permission from Ref. [159]. Copyright 2012 American Chemical Society)

The rattle-type nanoarchitectures, a special class of core-shell particles, have been extensively studied because of their unique structural properties and potential applications. These architectures possess spherical shells and solid cores having a variable space between them. Some rattle-type particles such as Au-polymer, SiO_2-Fe_2O_3 nanoball, and Cu-silica have been synthesized [157, 158]. Zhou et al. [159] fabricated rattle-type carbon-alumina core-shell spheres with large cavities and proposed a formation mechanism for them.

The time-dependent evolution of morphology was elucidated by TEM and it is shown in Fig. 6.12. The alumina-carbon composite microspheres were obtained via hydrothermal treatment before calcination. After calcination at 450 °C, the carbon transforms into carbon dioxide, meanwhile the loosely adsorbed Al^{3+} ions turn into dense Al_2O_3 network forming the shells of the rattle-type spheres [160]. A closer observation of the TEM images reveals that small cavities exist between the carbon cores and alumina shells resulting from the shrinkage during the calcination process. The formation mechanism of the rattle-type carbon-alumina particles was described as a two-step process. First, the carbohydrate used as a carbon precursor is subjected to dehydration, condensation, polymerization, and aromatization [161] and finally carbon spheres are formed. The surface of these carbon spheres is hydrophilic because it contains a considerable amount of reactive

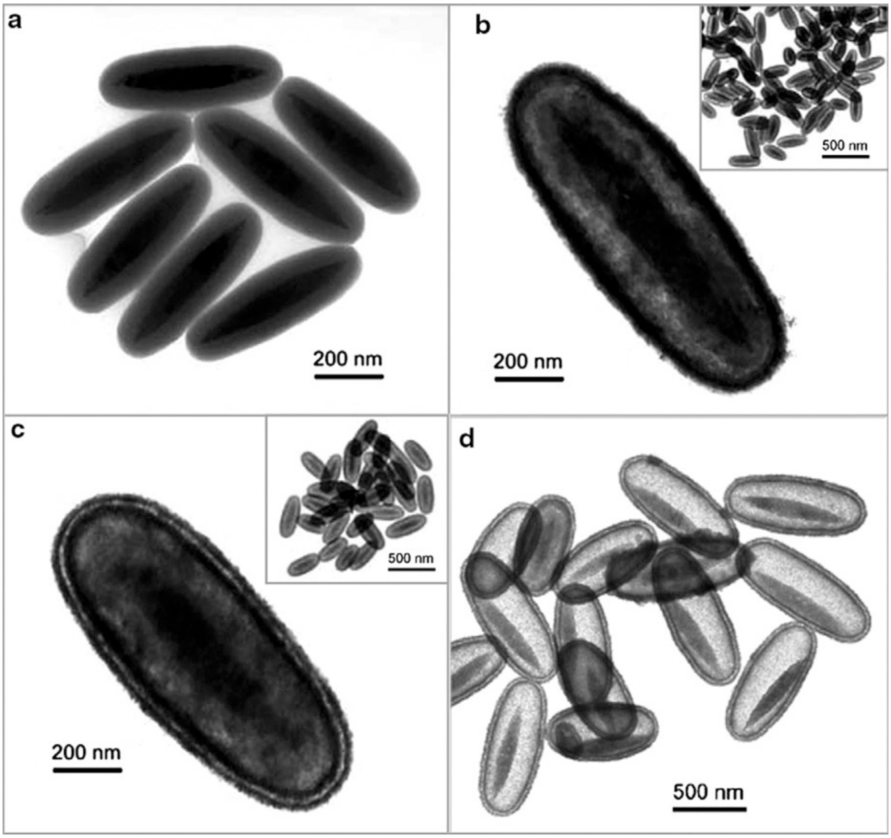

Fig. 6.13 TEM BF images of (**a**) α-Fe_2O_3/SiO_2 nanotemplates, (**b**) α-$Fe_2O_3/SiO_2/SnO_2$, (**c**) α-$Fe_2O_3/SiO_2/(SnO_2)_2$, (**d**) double-walled SnO_2 nano-cocoons with movable α-Fe_2O_3 spindles [46] (Reprinted with permission from Ref. [46]. Copyright 2007 Wiley-VCH)

oxygen-containing group. Therefore, Al^{3+} ions are easily attached to the surface of the carbon spheres. Second, 2 h calcinations result in the partial removal of carbon cores, and simultaneous densification and cross-linking of the incorporated aluminum ions in the shells, which leads to the formation of rattle-type structures.

Most work in this area was focused on spherical shape, and the resulting hollow spheres are generally single shelled. However, Lou et al. [46] reported a simple synthesis of double-walled SnO_2 ellipsoidal hollow nanoparticles with movable α-Fe_2O_3 cores. This method is based on hydrothermal shell-by-shell deposition of polycrystalline SnO_2 on ellipsoidal α-Fe_2O_3/SiO_2 nanotemplates. Firstly, α-Fe_2O_3 spindles were coated with a SiO_2 layer to produce ellipsoidal α-Fe_2O_3/SiO_2 core-shell particles (Fig. 6.13a). Then, two polycrystalline SnO_2 layers were deposited on the surface of the α-Fe_2O_3/SiO_2 core-shell particles through hydrothermal method. From Fig. 6.13c, a black core and double shell can be clearly distinguished. After annealing at 550 °C, the sandwiched silica layer is dissolved in sodium hydroxide solution to produce double-walled SnO_2 nano-cocoons (Fig. 6.13d). As can be seen from the image, most nano-cocoons encapsulate only one α-Fe_2O_3 spindle which is usually not located in the center of the cocoon. It is therefore believed that the encapsulated α-Fe_2O_3 spindle is free to move within each cocoon at least when filled with liquid.

5.2 Application of High-Angle Annular Dark-Field Imaging in Nanoparticles

The HAADF approach can detect the variation in chemical composition of the multicomponent sample with an atom-level resolution due to the enhanced contrast difference of various elements (Z-contrast imaging). The contrast of HAADF images is strongly dependent on the average atomic number of the scatterer encountered by the incident probe, not strongly affected by dynamical diffraction effects and defocus. Spatial resolution is limited by the size of the focused incident probe. So HAADF is suitable for characterization of core-shell nanomaterials. In the following we will discuss the application of HAADF images for characterization of core-shell nanomaterials, especially core-shell structured bimetallic nanoparticles [43, 162–170].

5.2.1 Au@Cu_2O Nanoparticles

Figure 6.14a and b shows typical HAADF images of the Au/Cu_2O nanocube heterostructures formed after heating copper grid in ambient environment. TEM observations show that nearly all the gold nanoparticles (>95 %) near the bars of copper grid have transformed into core-shell heterostructures. It can be clearly seen from Fig. 6.14a, b that the core is much brighter than the shell, which indicates that the core has a higher atomic number than that of the shell. Combined with energy-dispersive X-ray spectroscopy (EDS), the chemical compositions of the core and shell are determined to be Au and Cu_2O, respectively. In addition, there are two kinds of morphologies: one being a nearly perfect core-shell nanocube heterostructure and the other being formed through coalescence of two or more small particles (examples of the latter are indicated by white arrows in Fig. 6.14a). These two morphologies have nearly equal volume fractions. The edge dimensions of these heterostructures range from 15 to 45 nm, and the sizes of the cores range from 3.2 to 7.5 nm. TEM examinations of more than 200 core-shell heterostructures show that the edge length of a nanocube is proportional to the diameter of the particles at the core. The linear relationship between the core size and the edge length of the nanocubes is plotted in Fig. 6.14c. The linear relationship indicates that the gold core controls the growth of Cu_2O shell, acting as a template and catalyst. Figure 6.14d shows the SAED patterns taken from the pure Cu_2O nanocubes (the left half) and the Au-Cu_2O core-shell nanocube heterostructures (the right half). Due to the lattice parameter difference between Cu_2O ($a = 4.269$ Å) and gold ($a = 4.09$ Å), it can be seen that some rings (i.e., 111) in the right half are a little broadened.

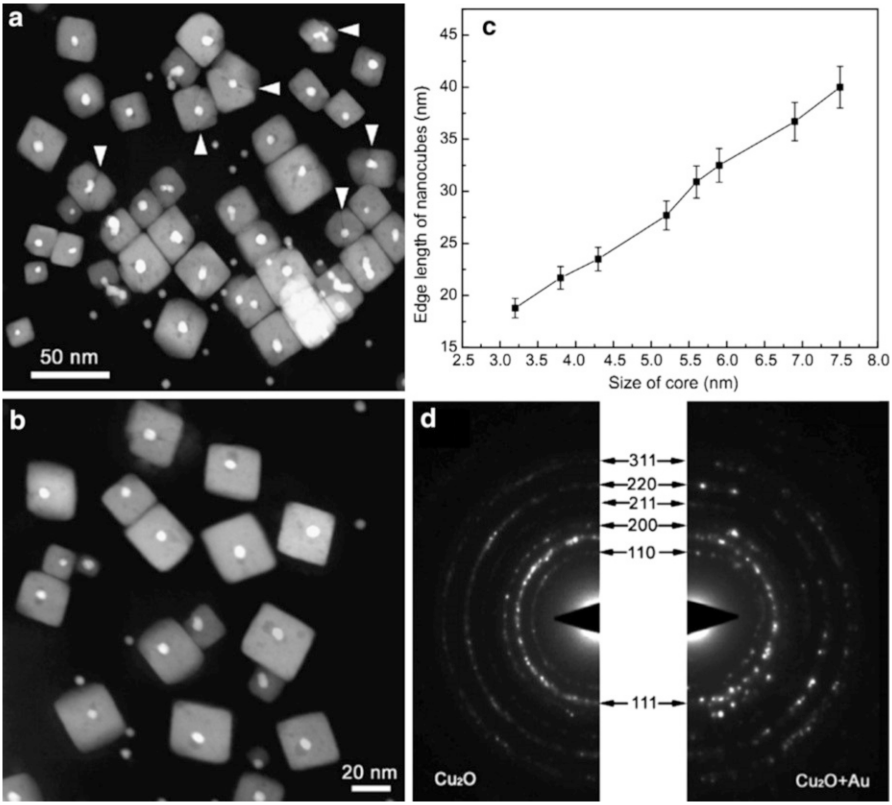

Fig. 6.14 (**a**, **b**) Typical HAADF images of core-shell nanocube heterostructures, showing two types of morphologies. (**c**) The relationship between the core sizes and the edge lengths of the nanocubes. (**d**) SAED patterns taken from the pure Cu_2O nanocubes and the Au-Cu_2O nanocube heterostructures [162] (Reprinted with permission from Ref. [162]. Copyright 2008 Elsevier Ltd.)

5.2.2 Metal@Metal Nanoparticles

Wu et al. [169] used HAADF techniques to observe the morphology of Au@Ag core-shell nanoparticles. As the atomic number difference between Ag(47) and Au (79) is sufficient, the Z-contrast imaging should be capable of distinguishing Au and Ag within the Au@Ag nanoparticles [171, 172]. The enlarged HAADF image in Fig. 6.15 shows that the Au core is brighter than Ag shell, and the Au@Ag core-shell nanoparticles could have various shapes such as cube, triangle, decahedron, and nanorod. Through careful analysis of Fig. 6.15, they found that the cubic Ag shells can form on Au cores with different shapes such as octahedral (Fig. 6.15a), truncated octahedral (Fig. 6.15b), and cubic (Fig. 6.15c). Single-twinned bi-triangular or bi-hexagonal Au cores predominated by {111}-type facets can epitaxially evolve into the single-twinned inverted bi-triangular Ag shells predominated by {100}-type facets (Fig. 6.15d, e). Decahedral Ag shells (Fig. 6.15f) are epitaxially overgrown from the decahedral Au cores and Ag shell

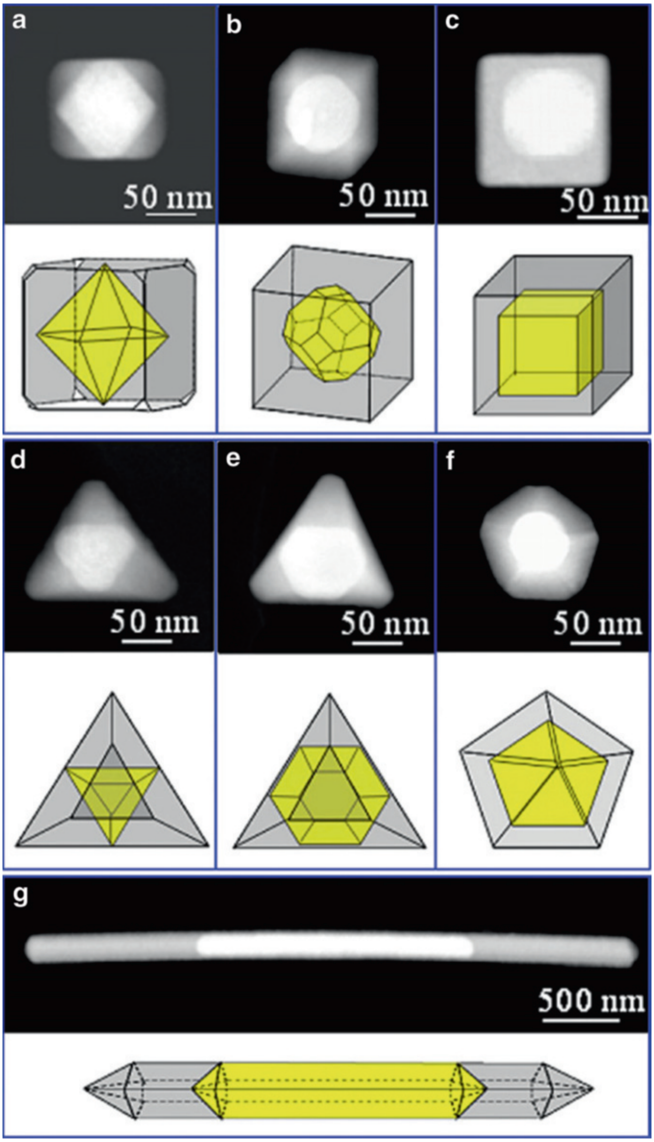

Fig. 6.15 The HAADF-STEM images of the individual Au@Ag nanoparticles with various shapes and their evolution models from different shaped Au core [169] (Reprinted with permission from Ref. [169]. Copyright 2009 IOP Publishing Ltd.)

nanorods (Fig. 6.15g) with a five-twinned cross section from the Au nanorod cores with the five-twinned cross section.

Serpell et al. [170] presented a new proof-of-concept method to synthesize core-shell nanoparticles in which ligand-based supramolecular forces are used to ensure

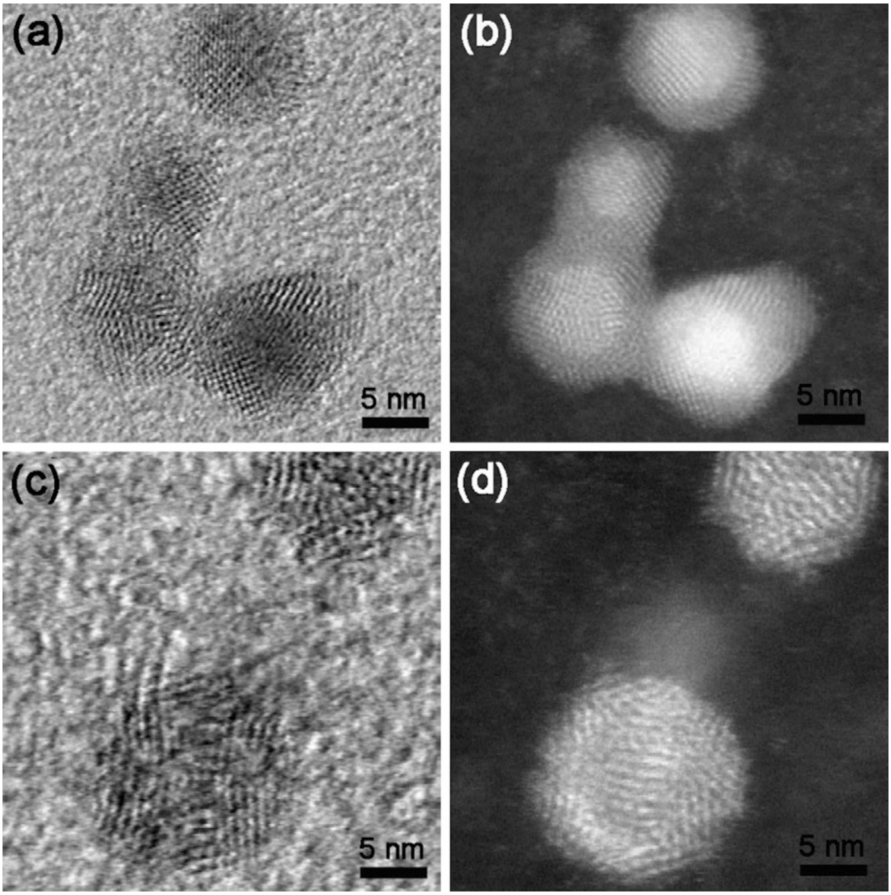

Fig. 6.16 HRTEM and aberration-corrected HAADF-STEM images of Au@Pd nanoparticles (**a**, **b**) and Pd@Au nanoparticles (**c**, **d**) [170] (Reprinted with permission from Ref. [170]. Copyright 2011 Nature Publishing Group)

surface segregation of the shell metal onto the preformed core before its reduction. They demonstrated the principle through the synthesis of Au@Pd, Pd@Au, Pt@Pd, and Pd@Pt nanoparticles using an anion coordination protocol. Conventional TEM instruments provide insufficient atomic number sensitivity for the determination of core-shell structure within the nanoparticles. Figure 6.16a, c is HRTEM images of Au@Pd and Pd@Au nanoparticles in which the lattice fringe images and the boundary between core and shell are not very clear. Therefore, aberration-corrected STEM with a HAADF detector was used to image the precise architectures of individual nanoparticles [173, 174]. The examination of Fig. 6.16b and d using a JEOL-2100F TEM/STEM with a probe correction and ~0.1 nm point resolution clearly reveals core-shell morphology. The intensity is directly related to the square of the atomic number of the elements, making Au atoms appear brighter relative to Pd. The image of Fig. 6.16b strikingly shows the Au core surrounded by a Pd coating at atomic resolution, with a regular crystalline structure. The Pd@Au nanoparticles appear to have a less regular crystalline structure than the Au@Pd nanoparticles, suggesting a modestly defined core-shell structure for this sample (Fig. 6.16d). This clearly illustrates that the structure within the nanoparticles can be modified by varying the reaction conditions.

Using aberration-corrected scanning transmission electron microscopy (STEM) and electron energy-loss spectroscopy (EELS) line profiles with Ångstrom resolution, Lin et al. [175] studied the structural changes of individual nanoparticles. After electrochemical dealloying, all of the dealloyed Pt-Ni nanoparticles revealed Pt-rich shells surrounding Pt-Ni alloy cores, as shown in Fig. 6.17. The EELS data evidence a distinct difference in the Ni distribution across the alloy cores. Figure 6.17a–d shows a typical high-resolution HAADF-STEM image and line scan EELS spectra across several nanoparticles of the D-PtNi catalyst. The Ni composition shows a monotonic decrease from the particle center to the particle surface. Contrary to that, the D-$PtNi_3$ catalyst (Fig. 6.17e–h) revealed an unusual Ni composition profile across the core, showing a previously undiscovered spherical enrichment of Ni at the near surface. Figure 6.17f, g presents two perpendicular EELS line scan profiles across the nanoparticle shown in Fig. 6.17e. Two off-center maxima of Ni intensity are clearly discernible in both directions, which coincide with the inflection points in the Pt intensity profiles. In other words, a Ni-enriched inner shell is formed near the surface and sandwiched between a Ni-poorer core and a Pt outer shell. This Ni-enriched inner shell is found to be universal in the D-$PtNi_3$ catalyst (Fig. 6.17h). In D-$PtNi_5$ catalyst (Fig. 6.17i–l), it is interesting to note that the Ni-enriched inner shell is located closer to the surface compared with D-$PtNi_3$. Figure 6.17j, k again shows two perpendicular EELS line scans from the nanoparticle shown in Fig. 6.17i, which display the Ni compositional maxima located closer to the surface compared with D-$PtNi_3$ catalyst.

Kim et al. [176] also used HAADF-STEM and EELS line profiles to study the structural changes of individual core-shell nanoparticles. Figure 6.18 shows the HAADF-STEM images and the cross-sectional compositional line profiles measured at the central (left panels) and edge parts (right panels) of $Pt_{0.97}Ag_{0.03}$, $Pt_{0.95}Ag_{0.05}$, $Pt_{0.90}Ag_{0.10}$, $Pt_{0.70}Ag_{0.30}$, and $Pt_{0.0}Ag_{1.0}$ nanoparticles. It can be seen that all the Pt@Ag particles were composed of Pt and Ag atoms. A closer examination reveals that the line profiles for $Pt_{0.97}Ag_{0.03}$, $Pt_{0.95}Ag_{0.05}$, $Pt_{0.90}Ag_{0.10}$, and $Pt_{0.70}Ag_{0.30}$ particles (Fig. 6.18a–d) are of the Pt core-Pt/Ag alloy shell types, while that of $Pt_{0.00}Ag_{1.00}$ particles are of a Pt core-Ag shell type (Fig. 6.18e). It is obvious that not all, but a substantial amount of seed Pt, has taken part in the formation of Pt/Ag alloys, except in the case of $Pt_{0.00}Ag_{1.00}$ nanoparticles.

5.3 Application of High-Resolution Transmission Electron Microscopy Imaging in Nanoparticles

HRTEM could provide a lot of useful information about the sample, such as crystallographic orientation, defects, and interfaces at an atomic scale.

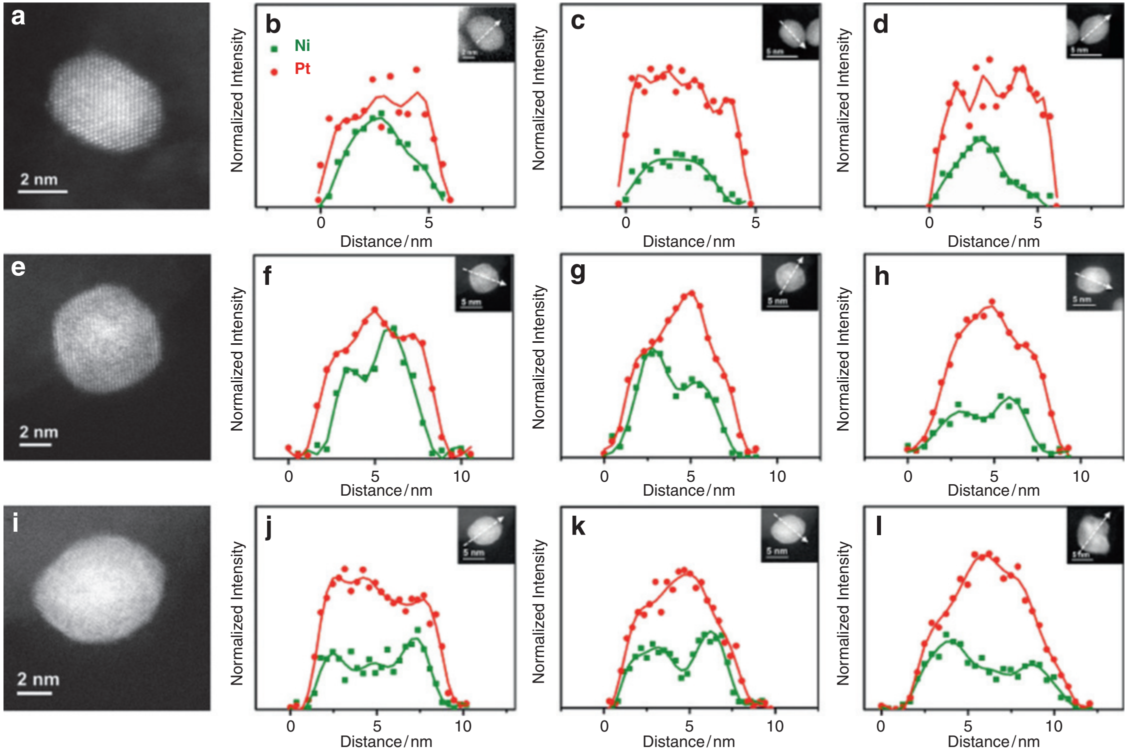

Fig. 6.17 High-resolution HAADF-STEM images and EELS compositional line profiles of individual D-PtNi (**a–d**), D-PtNi$_3$ (**e–h**), and D-PtNi$_5$ (**i–l**) nanoparticles. The directions of the line profiles were plotted as *dashed arrows* in the corresponding nanoparticles. The EELS profiles are normalized with the elemental scattering factors, and hence the intensity ratios represent thickness-projected compositions [175] (Reprinted with permission from Ref. [175]. Copyright 2012 American Chemical Society)

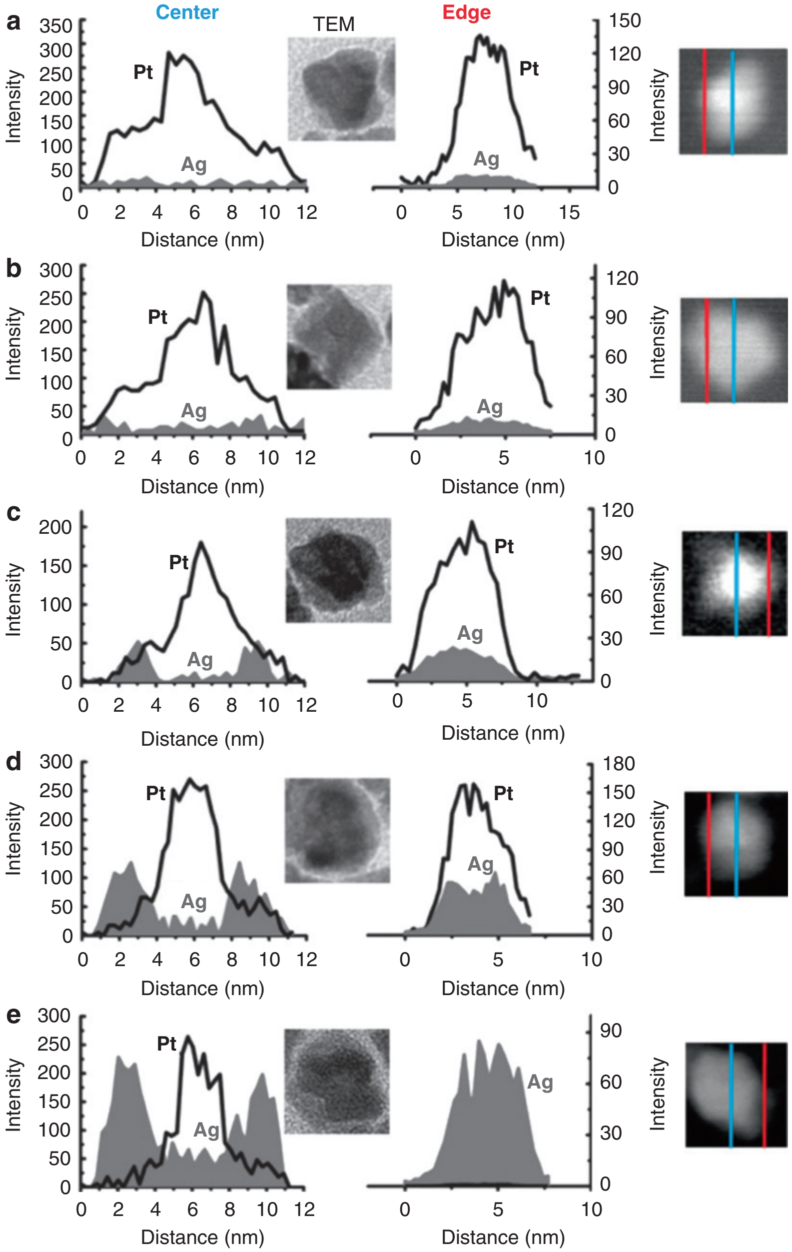

Fig. 6.18 HAADF-STEM images and cross-sectional compositional line profiles measured at the central (*left* panels) and edge parts (*right* panels) of (**a**) $Pt_{0.97}Ag_{0.03}$, (**b**) $Pt_{0.95}Ag_{0.05}$, (**c**) $Pt_{0.90}Ag_{0.10}$, (**d**) $Pt_{0.70}Ag_{0.30}$, and (**e**) $Pt_{0.0}Ag_{1.0}$ nanoparticles, each of which was grown on Pt seed particles [176] (Reprinted with permission from Ref. [176]. Copyright 2011 American Chemical Society)

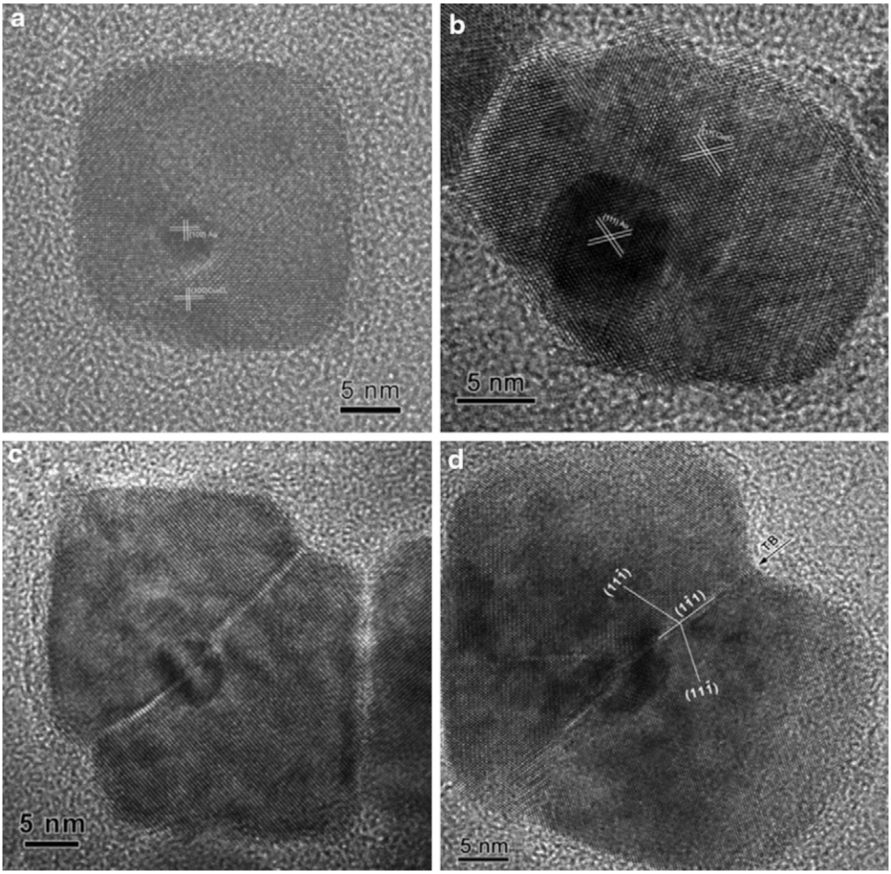

Fig. 6.19 (**a**) [001] zone-axis HRTEM image of a nearly perfect Au-Cu_2O nanocube heterostructure. (**b**) [011] zone-axis HRTEM image of a nearly perfect Au-Cu_2O nanocube heterostructure. (**c**) and (**d**) HRTEM images of coalesced Au-Cu_2O nanocube heterostructures [162] (Reprinted with permission from Ref. [162]. Copyright 2008 Elsevier Ltd.)

For core-shell structured nanomaterials, HRTEM images can illustrate the interface between core and shell. In the following, we will discuss the application of HRTEM image for characterization of core-shell nanomaterials [162, 177–184].

5.3.1 Au@Cu_2O Nanoparticles

In order to investigate the microstructure of Au@Cu_2O core-shell nanocubes, especially the interfaces between the gold nanoparticles and Cu_2O, Wang et al. [162] carried out systematic characterization of these nanoparticles by HRTEM. Most of the core-shell nanocube heterostructures demonstrate specific orientations of Au particle in Cu_2O cube. Figure 6.19 shows two major orientation relationships normally observed in these heterostructures: (a) [001]Au//[001]Cu_2O, {100}Au//{100}Cu_2O and (b) [011]Au//[011]Cu_2O, {111}Au//{111}Cu_2O. Contrary to the

HAADF images (Fig. 6. 14 in Sect. 5.2.1), the gold nanoparticle core has a dark contrast, while the Cu_2O shell has a light contrast. Figure 6.19a shows an example of a heterostructure in which gold nanoparticle and Cu_2O have an orientation relationship of [001]Au//[001]Cu_2O, {100}Au//{100}Cu_2O. However, the lattice is a little distorted around the interface due to the lattice misfit of about 4 % between Au and Cu_2O. Figure 6.19b shows an example of a heterostructure in which gold nanoparticle and Cu_2O have an orientation relationship of [011]Au//[011]Cu_2O, {111}Au//{111} Cu_2O. The {111} lattice misfit between Au and Cu_2O is about 2.3 %, which resulted in the lattice distortion around the interface. As mentioned earlier, some heterostructures are formed through coalescence of two or more small particles. Two examples are shown in Fig. 6.19c and d. Figure 6.19c shows an HRTEM image of a nanocube heterostructure formed through coalescence of two Cu_2O particles with a triangular shape. The boundary between two small particles is still evident. The final shape of this heterostructure is close to cubic. Figure 6.19d shows an HRTEM image of two coalesced particles with a trapezoid shape. The two particles coalesce through twinning, and the twinning configuration is indicated in Fig. 6.19d. Due to irregular shapes of the small particles, the final shape of the heterostructures is no longer cubic. The twinning configuration is thought to reduce the boundary energy and make the final structure more stable. It is believed that the presence of oxygen in the environment is crucial for the formation of Au-Cu_2O core-shell nanocube heterostructures since it can oxidize the copper into cuprous oxide at 300 °C.

5.3.2 PbTe/CdTe Core-Shell Nanoparticles

Core-shell quantum dots (QDs) are heterogeneous nanoparticles composed of an inorganic core enveloped by at least one inorganic shell of a second material. PbS/CdSe core-shell QDs can be prepared by cation exchange method [185]. Lambert et al. [183] demonstrated that the combination of the PbTe rock salt structure and the CdTe zinc blende structure allows for the direct observation of the core and the shell with HRTEM. This enables a direct visualization of the crystallographic properties of the PbTe/CdTe QDs and an evaluation of the cation exchange reaction. They observed a seamless match between the PbTe and CdTe crystal lattices and found that the formation of {111} terminated PbTe cores was favored. This intrinsic anisotropy of the exchange process leads to a strong increase in the heterogeneity of the cores formed, not only in terms of core size and shell thickness but also at the level of shape and position of the core.

Both PbTe and CdTe have a cubic structure [186] with almost no lattice mismatch (Fig. 6.20a, b). Since the appearance of the crystal lattice in HRTEM not only depends on the crystal orientation but also on the defocus, the same crystal plane may yield a different lattice image for both materials. Therefore, it is necessary to carry out a systematic HRTEM simulation. The simulated HRTEM images are shown in Fig. 6.20. When viewed along the <100> direction, PbTe and CdTe may yield two types of lattice images with a square symmetry (Fig. 6.20). The first has a lattice constant of 3.23 Å for PbTe (Fig. 6.20c) or 3.24 Å for CdTe (Fig. 6.20d); the second is tilted by 45° and has a lattice constant of 2.29 Å for both PbTe (Fig. 6.20e) and CdTe (Fig. 6.20f).

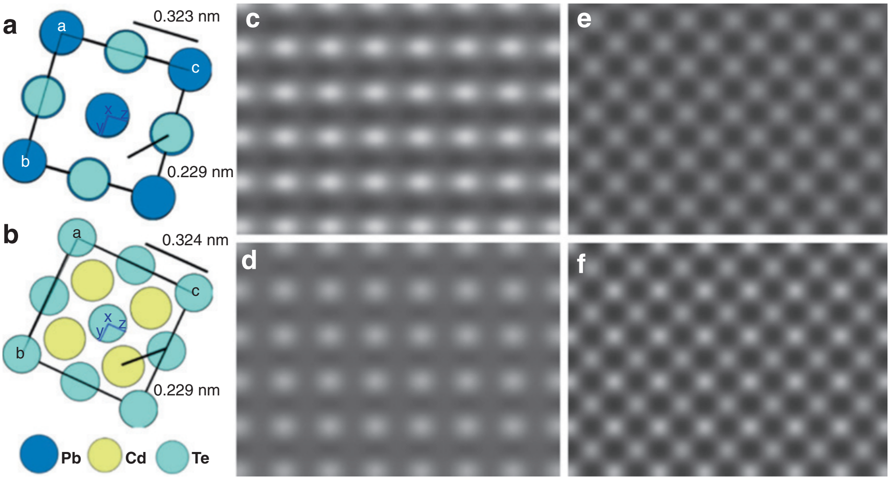

Fig. 6.20 Viewed along the <100> direction (**a**, **b**) structural models of PbTe and CdTe. (**c**, **e**) HRTEM simulation images of PbTe under different defocus. (**d**, **f**) HRTEM simulation images of CdTe under different defocus [183] (Reprinted with permission from Ref. [183]. Copyright 2009 American Chemical Society)

Figure 6.21 shows that resolved core-shell lattice images can be obtained in HRTEM for specific orientations of the particles. Viewed along the <100> direction, Fig. 6.21a represents an image where a core exhibits a 3.21 Å square pattern and a shell demonstrates a 2.34 Å square pattern. Both patterns are tilted by 45° and match seamlessly. By comparison with the simulated images, the core is determined to be PbTe and the shell is CdTe.

Along the <211> direction, PbTe and CdTe yield a rectangular lattice image with 2.29/1.94 Å and 3.89/2.29 Å unit cells, respectively. Figure 6.21b shows an image where both lattice images can be seen.

Along the <111> direction, the lattice images of both PbTe and CdTe show a hexagonal pattern with an almost identical lattice constant of 2.80 and 2.81 Å, respectively. Figure 6.21c gives an example of a PbTe/CdTe core-shell QD that exhibits this pattern. It appears as a simple, uniform particle with a continuously resolved lattice and no indication of any core-shell structure. This result is typical for all particles viewed along the <111> direction. It shows that the <111> axes of both core and shell point in the same direction, with a coherent alignment of {111} planes.

5.3.3 Zn/ZnO Core-Shell Nanobelts

ZnO nanomaterials can be used for fabricating nanolasers [187], field-effect transistors [188], gas sensors [189], nanocantilevers [190], and nanoresonators [191]. Wang et al. [184] synthesized heterostructured metal-semiconductor Zn-ZnO core-shell nanobelts successfully by a solid-vapor decomposition process [192]. The microstructure of epitaxial Zn-ZnO nanobelt has been studied by TEM.

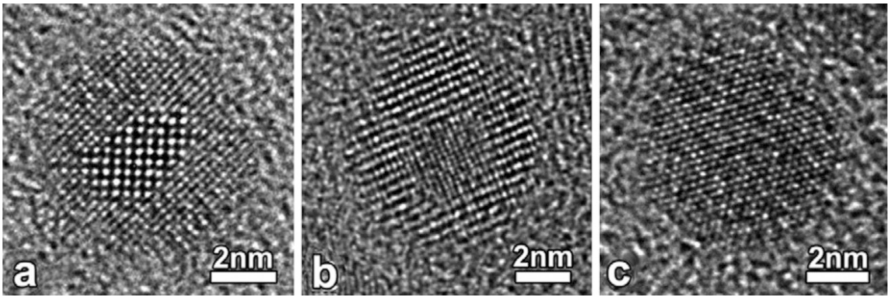

Fig. 6.21 HRTEM images of PbTe/CdTe core-shell particles in the (**a**) <100>, (**b**) <211>, and (**c**) <111> direction. A core-shell structure is observed only in the <100> and <211> direction [183] (Reprinted with permission from Ref. [183]. Copyright 2009 American Chemical Society)

Figure 6.22a is a low-magnification TEM image of the nanobelt, displaying a Zn-ZnO core-shell structure. The SAED pattern (Fig. 6.22c) indicates two sets of single-crystal diffraction spots, which are indexed to be [0001] Zn and [0001] ZnO with an epitaxial orientation. The weak reflection spots were produced by double diffractions from the core and the shell. Structurally, both Zn and ZnO have hexagonal crystal structure [193] with lattice constants of a = 2.665 Å, c = 4.947 Å and a = 3.249 Å, c = 5.206 Å, respectively, and the mismatch between the two in $\left(10\bar{1}0\right)$ is about 21.9 %. Therefore, the interference between the Bragg reflections from the two crystals produces Moiré fringes in the image, which are apparent in the HRTEM image in Fig. 6.22b at the region where the Zn core and the ZnO shell overlaps. However, in the region where there is only a ZnO shell, the HRTEM image shows clear lattice structure. The boundary between the Zn core and the ZnO shell is fairly sharp.

5.3.4 Pt@Pd Core-Shell Nanoparticles

Nguyen et al. [194] synthesized Pt@Pd core-shell nanoparticles and studied the structure of individual core-shell nanoparticles by HRTEM. Figure 6.23 shows the HRTEM images of Pt@Pd core-shell nanoparticles with the most characteristic polyhedral morphology and shape. The thin Pd shells grown over the Pt cores have led to form the core-shell configuration with the well-controlled size in the range of about 15–25 nm. The thickness of the coated shell was well controlled in the range of 1–3 nm. The Pt@Pd core-shell nanoparticles also show characteristic polyhedral morphology and shape, typically such as tetrahedral, octahedral, and cubes. Most of the Pt@Pd core-shell nanoparticles exhibit the low-index facets of {111}, {110}, and {100} planes.

5.4 Application of Elemental Mapping in Nanowires

Elemental mapping is based on inner-shell ionization of elements present in the sample giving rise to characteristic signals in well-defined energy-loss regions [195].

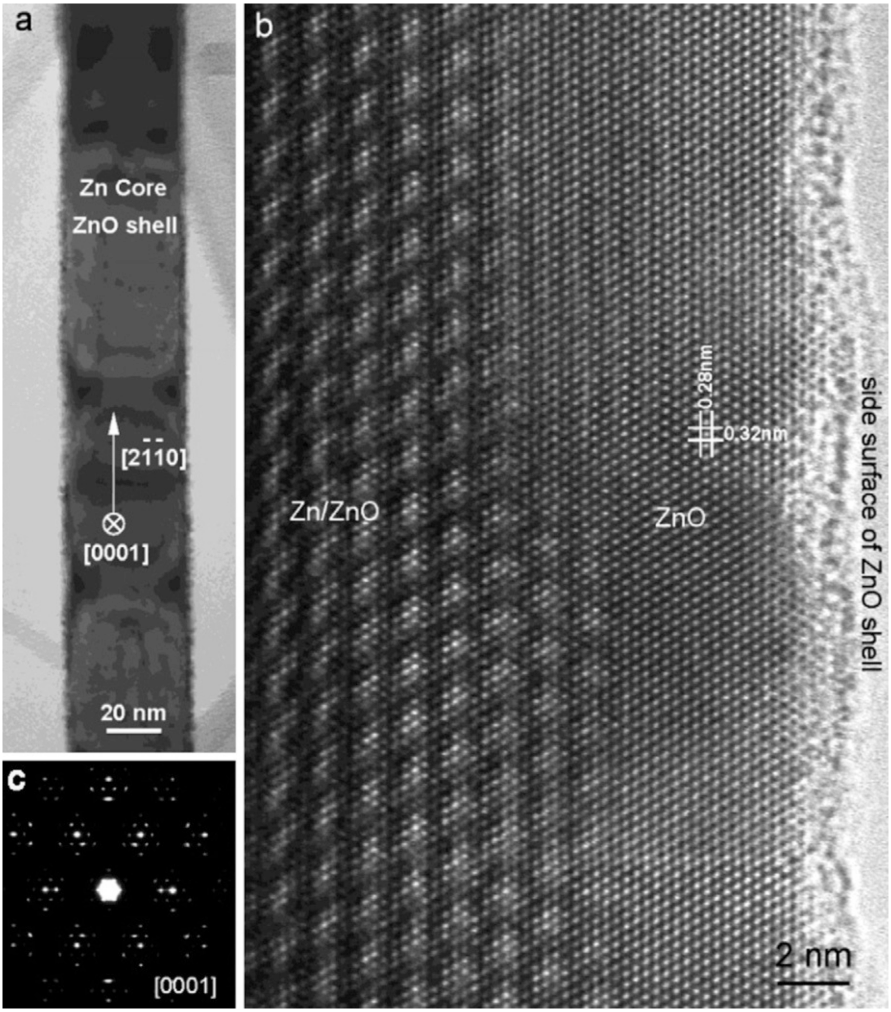

Fig. 6.22 (**a**) Low-magnification TEM image of a Zn-ZnO core-shell heteronanobelt. (**b**) [0001] HRTEM image recorded near the right-hand edge of a nanobelt, showing the Zn-ZnO overlapping region and the ZnO wall. (**c**) The corresponding SAED pattern [184] (Reprinted with permission from Ref. [184]. Copyright 2009 American Chemical Society)

It is a valuable tool for core-shell materials characterization. The applications of elemental mapping have spanned the range of research from biology to polymer materials [44, 196–199]. Elemental mapping, formed by imaging with electrons that have lost energies corresponding to inner-shell ionization edges for particular elements, can give the elemental distribution images in a relatively large area with high spatial resolution. In the following, we will discuss the application of elemental mapping for characterization of core-shell nanomaterials.

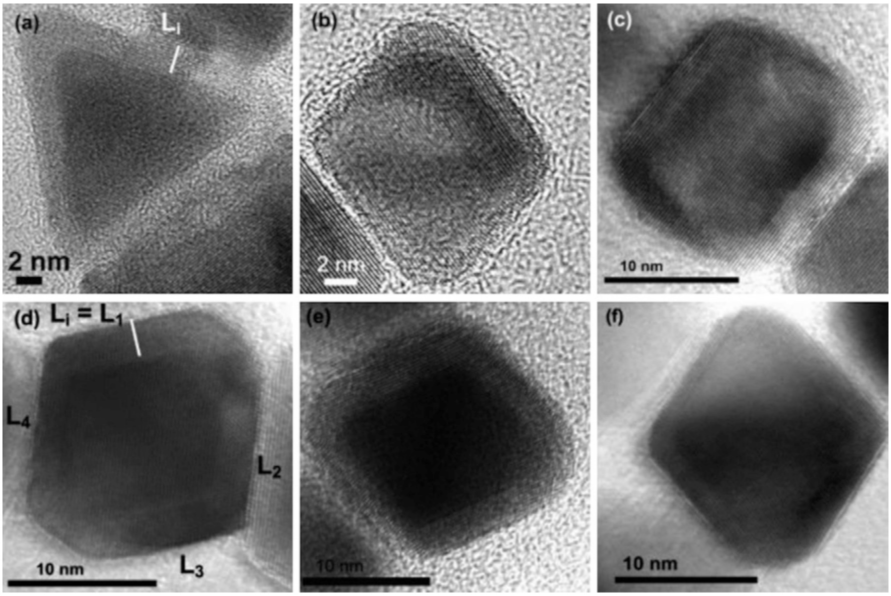

Fig. 6.23 (**a**–**e**) HRTEM images of Pt@Pd core-shell nanoparticles with the polyhedral morphology [194] (Reprinted with permission from Ref. [194]. Copyright 2009 American Chemical Society)

5.4.1 Boron@Boron Oxides Nanowires

It has been found that crystalline silicon [200] and germanium NWs [201] were sheathed with an amorphous oxide coating. Cao et al. [202] reported the successful synthesis of well-aligned straight amorphous boron NWs. From the HRTEM observation, it is difficult to detect whether there is an oxide coating layer of BO_x because the phase contrast of amorphous boron and amorphous BO_x coating cannot be easily distinguished. Therefore, it would be helpful to use the EFTEM. Wang et al. [197, 198] carried out a comprehensive characterization of boron NWs through EFTEM.

The aligned boron NWs were prepared by a radio-frequency magnetron sputtering method. A Philips CM200-FEG TEM equipped with a Gatan Imaging Filter (model 678) was used for elemental mapping and EELS examinations. A three-window method was used to study elemental distribution of boron and oxygen in order to clarify the existence of a boron oxide outer layer coating. The ionization edges selected for elemental mapping are listed as follows: B-K edge (188.5 eV) and O-K edge (532 eV). The exposure time for the elemental mapping of B and O was 10 and 20 s, and the width of the energy windows ΔE was set to be 10 and 20 eV, respectively. The EELS spectrum was acquired in the image mode with a half collection angle of ~13 mrad.

The EELS spectrum of single boron NW is shown in Fig. 6.24, revealing the characteristic boron K-shell ionization edges (~188 eV). Careful examination of

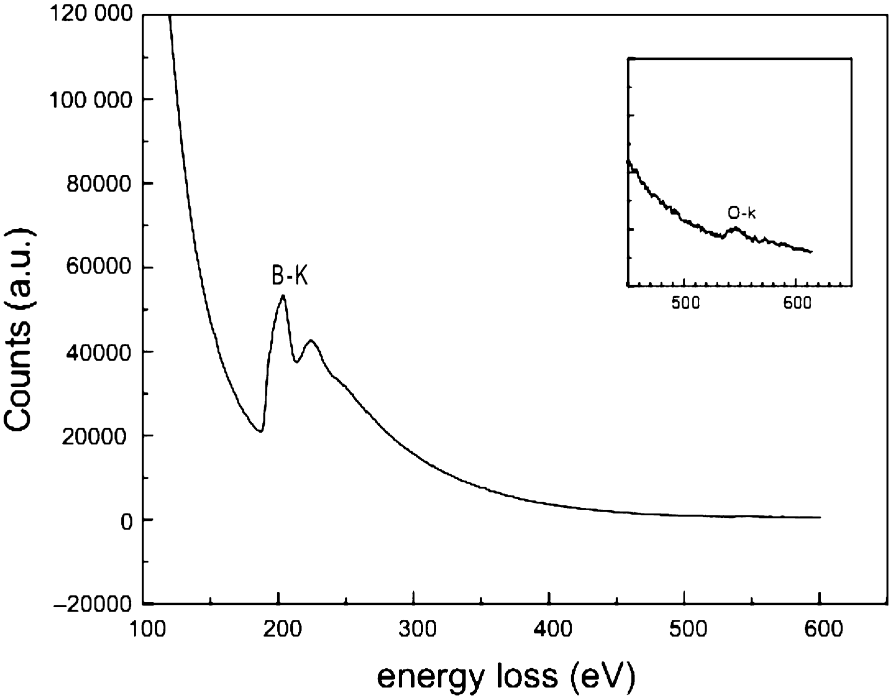

Fig. 6.24 EELS spectrum acquired from single boron nanowire (NW) showing strong boron K-shell peaks and a small peak at 532 eV corresponding to the oxygen K-edge [198] (Reprinted with permission from Ref. [198]. Copyright 2008 Elsevier Ltd.)

the EELS spectrum shows that a small peak is located at 532 eV, which corresponds to the K-shell excitation of oxygen. The magnified oxygen peak is shown in the inset of Fig. 6.24. This demonstrates that a small amount of oxygen exists in the boron NWs.

In order to further investigate the spatial distribution of boron and oxygen in the boron NWs, elemental mappings of boron and oxygen were achieved for the straight boron NWs (Fig. 6.25). It can be clearly seen that the boron is mainly distributed in the core (Fig. 6.25b), while oxygen is mainly located in the outer layer (Fig. 6.25c) of the boron NWs. The thickness of the outer oxidized layer is about 1–2 nm. The importance of oxide or oxygen for the both nucleation and growth of the boron NWs has been confirmed in an experiment (under the same conditions) using two targets (one is a mixture of B and B_2O_3, the other B only). The experiment showed that the quantity of NW stopped increasing after they switched the magnetron sputtering from the mixed target to the pure B target. Moreover, the diameter of the straight boron NWs (about 100 nm) using a pure B target is larger than that of the straight NWs (40–50 nm) using the mixed target.

In order to preclude the possibility of the oxidization layer after growth, some precautions were adopted. Before the boron NWs were put into TEM, they were

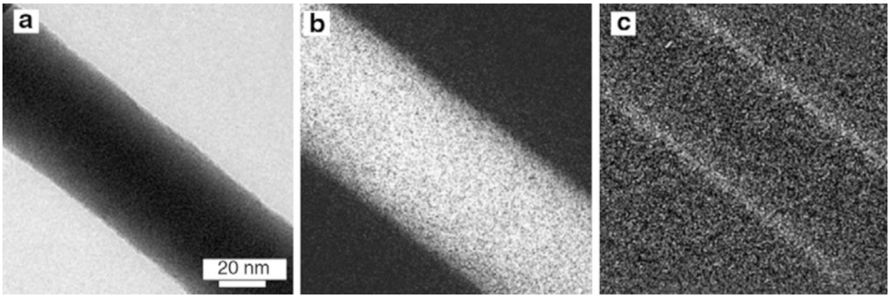

Fig. 6.25 (**a**) TEM image of single straight boron NW. (**b**) Elemental mapping of boron in the straight boron NW. (**c**) Elemental mapping of oxygen in the straight boron NW [198] (Reprinted with permission from Ref. [198]. Copyright 2008 Elsevier Ltd.)

kept in an argon atmosphere, not exposed to the air. The boron NWs were only exposed to air for several minutes during the TEM sample preparation. In addition, they carried out the oxygen mapping of the straight boron NWs (about 100 nm in diameter) produced by using a pure B target (without the oxygen source). The experimental results showed that there is no outer oxidized layer. So it is assured that the observed outer oxidized layer is not produced after growth. The oxide (B_2O_3) or oxygen is crucial for the nucleation and growth of the boron NWs.

5.4.2 Core-Multishell Semiconductor Nanowires

n-GaN/$In_xGa_{1\text{-}x}N$/GaN/*p*-AlGaN/*p*-GaN core-multishell NWs were synthesized by metal-organic chemical vapor deposition (MOCVD) [203], using a strategy involving axial elongation by nanocluster-catalyzed growth followed by controlled shell deposition onto the NW core [203]. To characterize the chemical composition and thickness of individual shells in the core-multishell heterostructures, Qian et al. [189] exploited cross-sectional imaging with the electron beam parallel (vs. perpendicular) to the NW axis since this allows for direct visualization of the spatial distribution of elements.

A cross-sectional BF TEM image (Fig. 6.26a) of a GaN/$In_xGa_{1\text{-}x}N$/GaN/AlGaN core-multishell NW taken along the $\left[11\overline{2}0\right]$ zone axis shows that the core-multishell wire has a triangular cross section with smooth facets. No dislocations or boundaries were observed in the NW, indicating an epitaxial deposition of the shells on the cores. Electron diffraction data (inset, Fig. 6.26a) further demonstrates that the core-multishell NW is single crystalline and that the three lateral facets can be indexed as (0001) and two $\left\{1\overline{1}0\overline{1}\right\}$ crystallographic planes. This result is consistent with the previous report on core/shell/shell NWs [203].

Additional analysis using STEM (Fig. 6.26b) revealed contrast indicative of variations in the radial chemical composition as expected for the core-multishell structure. STEM EDS mapping of the same NW region (Fig. 6.26c and e) confirmed the STEM results and defined clearly the spatial distributions of Ga, In, and Al in an individual shell that are consistent with targeted core-multishell structure. Interestingly, the thickness of InGaN shell was larger on the $\left(1\overline{1}0\overline{1}\right)$

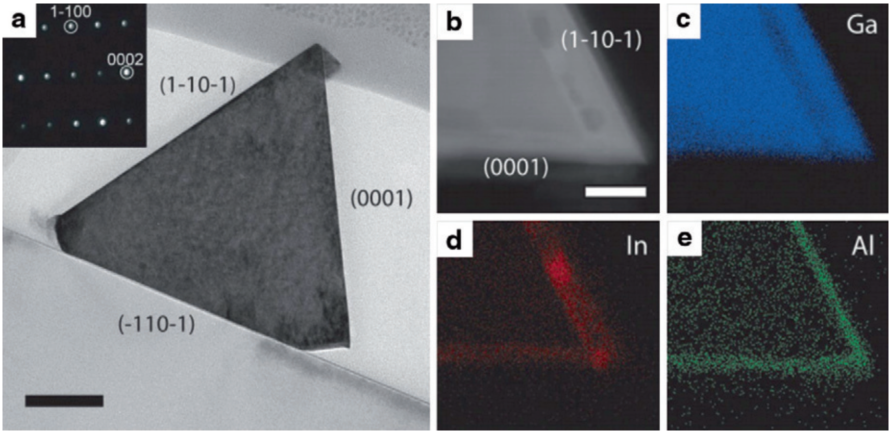

Fig. 6.26 TEM BF cross-section image of a GaN/In$_x$Ga$_{1-x}$/GaN/AlGaN core-multishell NW. Scale bar is 100 nm. *Inset*: $[11\overline{2}0]$ zone-axis SAED pattern. (**b**) STEM image recorded at a NW corner with (0001) and $(1\overline{1}0\overline{1})$ facets. Scale bar is 100 nm. (**c**–**e**) Elemental mapping of the same NW region, indicating spatial distribution of Ga (*blue*), In (*red*), and Al (*green*), respectively [44] (Reprinted with permission from Ref. [44]. Copyright 2008 American Chemical Society)

versus (0001) facet, indicating that shell deposition rate depends on the specific crystal planes. This can be understood in terms of different surface energies and polarities on nonequivalent facets [204] and suggests that these NWs could also serve as a model system to study growth kinetics. In addition, localized indium (In)-rich clusters on a scale of 10–50 nm were observed in the thicker InGaN layer grown on the $(1\overline{1}0\overline{1})$ facet. However, In segregation was not observed in the thinner layer grown on the (0001) facet. Similar In inhomogeneity has been reported in InGaN-based planar structures and is dependent on several factors, including InGaN layer thickness [205].

6 Conclusions and Future Perspective

This chapter concentrates on the introduction of various TEM techniques for characterization of core-shell nanomaterials. The objective was to review the versatility of TEM and the complimentary applications of the techniques. We take the TEM techniques as the clue to discuss the application of TEM for characterization of core-shell nanomaterials.

For TEM BF images, mass-thickness and diffraction contrast contribute to image formation: thick and crystalline areas appear with dark contrast. Since core-shell nanomaterials usually consist of different components, TEM BF image is applicable to most of them. We focus on three kinds of core-shell nanomaterials: silica coating core-shell nanomaterials, bimetallic core-shell nanomaterials, and hollow core-shell nanostructure. HAADF image is strongly dependent on the atomic number of the scatterer encountered by the incident probe, not strongly affected by dynamical diffraction effects or defocus conditions. So it has advantages in characterizing core-shell nanomaterials.

HRETM imaging process is very complicated and sensitive to the sample thickness and defocus conditions. HRTEM requires very thin TEM specimens free of preparation artifacts. Additionally, correct interpretation of HRTEM images requires systematic image simulations. Because of these limitations, only a small part of the core-shell nanomaterials can be characterized by HRTEM. But we can get lots of important information of core-shell nanomaterials through HRTEM image, such as orientation relationship and interface between the core and shell. So HRTEM is an effective characterization method, which cannot be ignored.

Elemental mapping combined with EELS can investigate the spatial distribution of elements in the nanomaterials. Especially when the core and shell has a same structure and similar atomic numbers, the three methods mentioned above cannot distinguish.

BF image, HADDF image, HRTEM image, and elemental mapping are the most popular and effective methods for the characterization of core-shell nanomaterials. In fact, other TEM techniques can also be used to investigate core-shell nanomaterials, such as TEM dark-field image and SAED. With the development of TEM techniques, the microstructure of core-shell nanomaterials can be studied in more detail.

Acknowledgment The authors would like to thank the financial support from the National Natural Science Foundation of China (Grant Nos. 10974105), the National Basic Research Program of China (Grant No. 2012CB722705), the Natural Science Foundation for Outstanding Young Scientists in Shandong Province (Grant No. JQ201002), the Project of Introducing Talents to Support Thousand Talents Programs (Grant No. P201101032), the Program of Science and Technology in Qingdao City (Grant No. 11-2-4-23-hz), and the Scientific Research Starting Foundation for the Introduced Talents at Qingdao University (Grant No. 06300701). Y. Q. Wang would also like to thank the financial support from the Taishan Outstanding Overseas Scholar Program in Shandong Province.

References

1. Henglein A (1989) Small-particle research: physicochemical properties of extremely small colloidal metal and semiconductor particles. Chem Rev 89(8):1861–1873
2. Spanhel L, Weller H, Henglein A (1987) Photochemistry of semiconductor colloids. 22. Electron ejection from illuminated cadmium sulfide into attached titanium and zinc oxide particles. J Am Chem Soc 109(22):6632–6635
3. Youn HC, Baral S, Fendler JH (1988) Dihexadecyl phosphate, vesicle-stabilized and in situ generated mixed cadmium sulfide and zinc sulfide semiconductor particles: preparation and utilization for photosensitized charge separation and hydrogen generation. J Phys Chem 92(22):6320–6327
4. Hoener CF, Allan KA, Bard AJ, Campion A et al (1992) Demonstration of a shell-core structure in layered cadmium selenide-zinc selenide small particles by x-ray photoelectron and Auger spectroscopies. J Phys Chem 96(9):3812–3817

5. Honma I, Sano T, Komiyama H (1993) Surface-enhanced Raman scattering (SERS) for semiconductor microcrystallites observed in silver-cadmium sulfide hybrid particles. J Phys Chem 97(25):6692–6695
6. Zhou HS, Sasahara H, Honma I, Komiyama H et al (1994) Coated semiconductor nanoparticles: the CdS/PbS system's photoluminescence properties. Chem Mater 6(9):1534–1541
7. Ahmed J, Sharma S, Ramanujachary KV, Lofland SE et al (2009) Microemulsion-mediated synthesis of cobalt (pure fcc and hexagonal phases) and cobalt-nickel alloy nanoparticles. J Colloid Interface Sci 336(2):814–819
8. El-Safty SA (2008) Synthesis, characterization and catalytic activity of highly ordered hexagonal and cubic composite monoliths. J Colloid Interface Sci 319(2):477–488
9. Song Q, Zhang ZJ (2004) Shape control and associated magnetic properties of spinel cobalt ferrite nanocrystals. J Am Chem Soc 126(19):6164–6168
10. Salazar-Alvarez G, Qin J, Sépelák V, Bergmann I et al (2008) Cubic versus spherical magnetic nanoparticles: the role of surface anisotropy. J Am Chem Soc 130(40):13234–13239
11. Schmidt E, Vargas A, Mallat T, Baiker A (2009) Shape-selective enantioselective hydrogenation on Pt nanoparticles. J Am Chem Soc 131(34):12358–12367
12. Wang ZL, Ahmad TS, El-Sayed MA (1997) Steps, ledges and kinks on the surfaces of platinum nanoparticles of different shapes. Surf Sci 380(2–3):302–310
13. Wei XW, Zhu GX, Liu YJ, Ni YH et al (2008) Large-scale controlled synthesis of FeCo nanocubes and microcages by wet chemistry. Chem Mater 20(19):6248–6253
14. Yamade M, Kon S, Miyake M (2005) Synthesis and size control of Pt nanocubes with high selectivity using the additive effect of NaI. Chem Lett 34(7):1050–1051
15. Hu JS, Guo YG, Liang HP, Wan LJ et al (2005) Three-dimensional self-organization of supramolecular self-assembled porphyrin hollow hexagonal nanoprisms. J Am Chem Soc 127(48):17090–17095
16. Jitianu M, Goia DV (2007) Zinc oxide colloids with controlled size, shape, and structure. J Colloid Interface Sci 309(1):78–85
17. Ren TZ, Yuan ZY, Hu WK, Zou XD (2008) Single crystal manganese oxide hexagonal plates with regulated mesoporous structures. Micropor Mesopor Mater 112(1–3):467–473
18. Ren XL, Han D, Chen D, Tang FQ (2007) Large-scale synthesis of hexagonal cone-shaped ZnO nanoparticles with a simple route and their application to photocatalytic degradation. Mater Res Bull 42(5):807–813
19. Suematsu NJ, Ogawa Y, Yamamoto Y, Yamaguchi T (2007) Dewetting self-assembly of nanoparticles into hexagonal array of nanorings. J Colloid Interface Sci 310(2):648–652
20. Wu L, Yu JC, Zhang LZ, Wang XC et al (2004) Selective self-propagating combustion synthesis of hexagonal and orthorhombic nanocrystalline yttrium iron oxide. J Solid State Chem 177(10):3666–3674
21. Qu XZ, Omar L, Le TBH, Tetley L et al (2008) Polymeric amphiphile branching leads to rare nanodisc shaped planar self-assemblies. Langmuir 24(18):9997–10004
22. Cao GZ, Liu DW (2008) Template-based synthesis of nanorod, nanowire, and nanotube arrays. Adv Colloids Interface Sci 136(1–2):45–64
23. Kline TR, Tian ML, Wang JG, Sen A et al (2006) Template-grown metal nanowires. Inorg Chem 45(19):7555–7565
24. Li MW, Mayer TS, Sioss JA, Keating CD et al (2007) Template-grown metal nanowires as resonators: performance and characterization of dissipative and elastic properties. Nano Lett 7(11):3218–3284
25. Liu Z, Elbert D, Chien CL, Searson PC (2008) FIB/TEM characterization of the composition and structure of core/shell Cu-Ni nanowires. Nano Lett 8(8):2166–2170
26. Peña DJ, Mbindyo JKN, Carado AJ, Mallouk TE et al (2002) Template growth of photoconductive metal-CdSe-metal nanowires. J Phys Chem B 106(30):7458–7462

27. Routkevitch D, Bigioni T, Moskovits M, Xu JM (1996) Electrochemical fabrication of CdS nanowire arrays in porous anodic aluminum oxide templates. J Phys Chem 100(33):14037–14047
28. Sioss JA, Keating CD (2005) Batch preparation of linear Au and Ag nanoparticle chains via wet chemistry. Nano Lett 5(9):1779–1783
29. Wu YY, Livneh T, Zhang YX, Cheng GS et al (2004) Templated synthesis of highly ordered mesostructured nanowires and nanowire arrays. Nano Lett 4(12):2337–2342
30. Bok HM, Kim S, Yoo SH, Kim SK et al (2008) Synthesis of perpendicular nanorod arrays with hierarchical architecture and water slipping superhydrophobic properties. Langmuir 24(8):4168–4173
31. Bok HM, Shuford KL, Kim S, Kim SK et al (2008) Multiple surface plasmon modes for a colloidal solution of nanoporous gold nanorods and their comparison to smooth gold nanorods. Nano Lett 8(8):2265–2270
32. Nicewarner-Peña SR, Freeman RG, Reiss BD, He L et al (2001) Submicrometer metallic barcodes. Science 294(5540):137–141
33. Park S, Chung SW, Mirkin CA (2004) Hybrid organic-inorganic, rod-shaped nanoresistors and diodes. J Am Chem Soc 126(38):11772–11773
34. Park S, Lim JH, Chung SW, Mirkim CA (2004) Self-assembly of mesoscopic metal-polymer amphiphiles. Science 303(5656):348–351
35. Paxton WF, Kistler KC, Olmeda CC, Sen A et al (2004) Catalytic nanomotors: autonomous movement of striped nanorods. J Am Chem Soc 126(41):13424–13431
36. Peng XG, Manna L, Yang WD, Wickham J et al (2000) Shape control of CdSe nanocrystals. Nature 404(6673):59–61
37. Yoo SH, Park S (2007) Platinum-coated, nanoporous gold nanorod arrays: synthesis and characterization. Adv Mater 19(12):1612–1615
38. Michailowski A, Almawlawi D, Cheng GS, Moskovits M (2001) Highly regular anatase nanotubule arrays fabricated in porous anodic templates. Chem Phys Lett 349(1–2):1–5
39. Shelimov KB, Moskovits M (2000) Composite nanostructures based on template-grown boron nitride nanotubules. Chem Mater 12(1):250–254
40. Shin TY, Yoo SH, Park S (2008) Gold nanotubes with a nanoporous wall: their ultrathin platinum coating and superior electrocatalytic activity toward methanol oxidation. Chem Mater 20(17):5682–5686
41. Xiao R, Cho SI, Liu R, Lee SB (2007) Controlled electrochemical synthesis of conductive polymer nanotube structures. J Am Chem Soc 129(14):4483–4489
42. Ge JP, Zhang Q, Zhang TR, Yin YD (2008) Core-satellite nanocomposite catalysts protected by a porous silica shell: controllable reactivity, high stability, and magnetic recyclability. Angew Chem Int Ed 120(47):8924–8928
43. Ferrer D, Torres-Castro A, Gao X, Sepúlveda-Guzmán S et al (2007) Three-layer core/shell structure in Au-Pd bimetallic nanoparticles. Nano Lett 7(6):1701–1705
44. Qian F, Gradečak S, Li Y, Wen CY et al (2005) Core/multishell nanowire heterostructures as multicolor, high-efficiency light-emitting diodes. Nano Lett 5(11):2287–2291
45. Liu J, Xia H, Xue DF, Lu L (2009) Double-shelled nanocapsules of V_2O_5-based composites as high-performance anode and cathode materials for Li ion batteries. J Am Chem Soc 131(34):12086–12087
46. Lou XW, Yuan C, Archer LA (2007) Double-walled SnO_2 nano-cocoons with movable magnetic cores. Adv Mater 19(20):3328–3332
47. Lee KT, Jung YS, Oh SM (2003) Synthesis of tin-encapsulated spherical hollow carbon for anode material in lithium secondary batteries. J Am Chem Soc 125(19):5652–5653
48. Kalele S, Gosavi SW, Urban J, Kulkami SK (2006) Nanoshell particles: synthesis, properties and applications. Curr Sci 91(8):1038–1052
49. Balakrishnan S, Bonder MJ, Hadjipanayis GC (2009) Particle size effect on phase and magnetic properties of polymer-coated magnetic nanoparticles. J Magn Magn Mater 321(2):117–122

50. Kim MJ, Choa YH, Kim DH, Kim KH (2009) Magnetic behaviors of surface modified superparamagnetic magnetite nanoparticles. IEEE Trans Magn 45(6):2446–2449
51. Laurent S, Forget D, Port M, Roch A et al (2008) Magnetic iron oxide nanoparticles: synthesis, stabilization, vectorization, physicochemical characterizations, and biological applications. Chem Rev 108(6):2064–2110
52. Salgueiriño-Maceira V, Correa-Duarte MA (2007) Increasing the complexity of magnetic core/shell structured nanocomposites for biological applications. Adv Mater 19(23):4131–4144
53. Caruso F (2001) Nanoengineering of particle surfaces. Adv Mater 13(1):11–22
54. Daniel MC, Astruc D (2004) Gold nanoparticles: assembly, supramolecular chemistry, quantum-size-related properties, and applications toward biology, catalysis, and nanotechnology. Chem Rev 104(1):293–346
55. Phadtare S, Kumar A, Vinod VP, Dash C et al (2003) Direct assembly of gold nanoparticle "shells" on polyurethane microsphere "cores" and their application as enzyme immobilization templates. Chem Mater 15(10):1944–1949
56. Kortan AR, Hull R, Opila RL, Bawendi MG et al (1990) Nucleation and growth of cadmium selenide on zinc sulfide quantum crystallite seeds, and vice versa, in inverse micelle media. J Am Chem Soc 112(4):1327–1332
57. Qi LM, Ma JM, Cheng HM, Zhao ZG (1996) Synthesis and characterization of mixed CdS-ZnS nanoparticles in reverse micelles. Colloids Surf A: Physicochem Eng Asp 111(3):195–202
58. Mews A, Eychmueller A, Giersig M, Schooss D et al (1994) Preparation, characterization, and photophysics of the quantum dot quantum well system cadmium sulfide/mercury sulfide/cadmium sulfide. J Phys Chem 98(3):934–941
59. Ma GH, He J, Rajiv K, Tang SH et al (2004) Observation of resonant energy transfer in Au:CdS nanocomposite. Appl Phys Lett 84(23):4684–4686
60. Kamat PV, Shanghavi B (1997) Interparticles electron transfer in metal/semiconductor composites. picosecond dynamics of CdS-capped gold nanoclusters. J Phys Chem B 101(39):7675–7679
61. Scodeller P, Flexer V, Szamocki R, Calvo EJ (2008) Wired-enzyme core-shell Au nanoparticle biosensor. J Am Chem Soc 130(38):12690–12697
62. Babes L, Denizot B, Tanguy G, Jacques J (1999) Synthesis of iron oxide nanoparticles used as MRI contrast agents: a parametric study. J Colloid Interface Sci 212(2):474–482
63. de Farias PMA, Santos BS, Menezes FD, Brasil AG Jr et al (2007) Highly fluorescent semiconductor core-shell CdTe-CdS nanocrystals for monitoring living yeast cells activity. Appl Phys Mater Sci Process 89(4):957–961
64. de Menezes FD, Brasil AG Jr, Moreira WL, Barbosa LC et al (2005) CdTe/CdS core shell quantum dots for photonic applications. Microelectron J 36(11):989–991
65. Gupta AK, Gupta M (2005) Synthesis and surface engineering of iron oxide nanoparticles for biomedical applications. Biomaterials 26(18):3995–4021
66. Schreder B, Schmidt T, Ptatschek V, Spanhel L (2000) Raman characterization of CdTe/CdS-"core-shell"-clusters in colloids and films. J Cryst Growth 214–215(2):782–786
67. Zimmer JP, Kim SW, Ohnishi S, Tanaka E et al (2006) Size series of small indium arsenide-zinc selenide core-shell nanocrystals and their application to in vivo imaging. J Am Chem Soc 128(8):2526–2527
68. Dresco PA, Zaitsev VS, Gambino RJ, Chu B (1999) Preparation and properties of magnetite and polymer magnetite nanoparticles. Langmuir 15(6):1945–1951
69. Sounderya N, Zhang Y (2010) Use of core/shell structured nanoparticles for biomedical applications. Recent Patents Biomed Eng 1(1):34–42
70. Yan E, Ding Y, Chen CJ, Li R et al (2009) Polymer/silica hybrid hollow nanospheres with pH-sensitive drug release in physiological and intracellular environments. Chem Commun 45(19):2718–2720
71. Michalet X, Pinaud FF, Bentolila LA, Tsay JM et al (2005) Quantum dots for live cells, in vivo imaging, and diagnostics. Science 307(5709):538–544

72. De M, Ghosh PS, Rotello VM (2008) Applications of nanoparticles in biology. Adv Mater 20(22):4225–4241
73. Williams DB, Carter CB (1996) Transmission electron microscopy. Springer, New York
74. Subramanian R, Denney PE, Singh J, Otooni M (1998) A novel technique for synthesis of silver nanoparticles by laser-liquid interaction. J Mater Sci 33(13):3471–3477
75. Kumar P, Kumar R, Kanjilal D, Knobel M et al (2008) Ion beam synthesis of Ni nanoparticles embedded in quartz. J Vac Sci Technol B 26(4):36–40
76. Li H, Vilar RM, Wang YM (1997) Laser beam processing of a SiC particulate reinforced 6061 aluminium metal matrix composite. J Mater Sci 32(20):5545–5550
77. Dodd AC (2009) A comparison of mechanochemical methods for the synthesis of nanoparticulate nickel oxide. Powder Technol 196(1):30–35
78. Deng WJ, Xia W, Li C, Tang Y (2009) Formation of ultra-fine grained materials by machining and the characteristics of the deformation fields. J Mater Process Technol 209(9):4521–4526
79. Sasikumar R, Arunachalam RM (2009) Synthesis of nanostructured aluminium matrix composite (AMC) through machining. Mater Lett 63(28):2426–2428
80. Sneh O, Clark-Phelps RB, Londergan AR, Winkler J et al (2002) Thin film atomic layer deposition equipment for semiconductor processing. Thin Solid Films 402(1–2):248–261
81. Wang YY, Cai KF, Yao X (2009) Facile synthesis of PbTe nanoparticles and thin films in alkaline aqueous solution at room temperature. J Solid State Chem 182(12):3383–3386
82. Yoo SH, Liu LC, Park S (2009) Nanoparticle films as a conducting layer for anodic aluminum oxide template-assisted nanorod synthesis. J Colloid Interface Sci 339(1):183–186
83. Ye J, de Broed BV, Palma RD, Libaers W et al (2008) Surface morphology changes on silica-coated gold colloids. Colloids Surf A: Physicochem Eng Asp 322(1–3):225–233
84. Qi YL, Chen M, Liang S, Yang W et al (2008) Micro-patterns of Au@SiO_2 core-shell nanoparticles formed by electrostatic interactions. Appl Surf Sci 254(6):1684–1690
85. Qi YL, Chen M, Liang S, Zhao J et al (2007) Hydrophobation and self-assembly of core-shell Au@SiO_2 nanoparticles. Colloids Surf A: Physicochem Eng Aspects 302(1–3):383–387
86. Poovarodom S, Bass JD, Hwang SJ, Katz A (2005) Investigation of the core-shell interface in gold@silica nanoparticles: a silica imprinting approach. Langmuir 21(26):12348–12356
87. Lu Y, Yin YD, Li ZY, Xia YN (2002) Synthesis and self-assembly of Au@SiO_2 core-shell colloids. Nano Lett 2(7):785–788
88. Alejandro-Arellano M, Ung T, Blanco Á, Mulvaney P (2000) Silica-coated metals and semiconductors. Stabilization and nanostructuring. Pure Appl Chem 72(1–2):257–268
89. Li T, Moon J, Morrone AA, Mecholsky JJ et al (1999) Preparation of Ag/SiO_2 nanosize composites by a reverse micelle and sol-gel technique. Langmuir 15(13):4328–4334
90. Fu WY, Yang HB, Chang LX, Li MH et al (2005) Preparation and characteristics of core-shell structure nickel/silica nanoparticles. Colloids Surf A: Physicochem Eng Aspects 262(1–3):71–75
91. Lu XG, Liang GY, Sun ZB, Zhang W (2005) Ferromagnetic Co/SiO_2 core/shell structured nanoparticles prepared by a novel aqueous solution method. Mater Sci Eng B 117(2):147–152
92. Cha HJ, Kim YH, Cha HG, Kang YS (2007) Preparation and characterization of Ag (core)/ SiO_2 (shell) nanoparticles. Surf Rev Lett 14(4):693–696
93. Kanehara M, Watanabe Y, Teranishi T (2009) Thermally stable silica-coated hydrophobic gold nanoparticles. J Nanosci Nanotechnol 9(1):673–675
94. Ma ZY, Dosev D, Nichkova M, Dumas RK et al (2009) Synthesis and characterization of multifunctional silica core-shell nanocomposites with magnetic and fluorescent functionalities. J Magn Magn Mater 321(10):1368–1371
95. Mazaleyrat F, Ammar M, LoBue M, Bonnet JP et al (2009) Silica coated nanoparticles: synthesis, magnetic properties and spin structure. J Alloys Compd 483(1–2):473–478

96. Dong BH, Cao LX, Su G, Liu W et al (2009) Synthesis and characterization of the water-soluble silica-coated ZnS:Mn nanoparticles as fluorescent sensor for Cu^{2+} ions. J Colloid Interface Sci 339(1):78–82
97. Ammar M, Mazaleyrat F, Bonnet JP, Audebert P et al (2007) Synthesis and characterization of core-shell structure silica-coated Fe29.5Ni70.5 nanoparticles. Nanotechnology 18(28):285606
98. Lee J, Lee YJ, Youn JK, Na HB et al (2008) Simple synthesis of functionalized superparamagnetic magnetite/silica core/shell nanoparticles and their application as magnetically separable high-performance biocatalysts. Small 4(1):143–152
99. Aliev FG, Correa-Duarte MA, Mamedov A, Ostrander JW et al (1999) Layer-by-layer assembly of core-shell magnetite nanoparticles: effect of silica coating on interparticle interactions and magnetic properties. Adv Mater 11(12):1006–1010
100. Lien YH, Wu TM (2008) Preparation and characterization of thermosensitive polymers grafted onto silica-coated iron oxide nanoparticles. J Colloid Interf Sci 326(2):517–521
101. He R, You XG, Shao J, Gao F et al (2007) Core/shell fluorescent magnetic silica-coated composite nanoparticles for bioconjugation. Nanotechnology 18(31):315601
102. Correa-Duarte MA, Giersig M, Liz-Marzán LM (1998) Stabilization of CdS semiconductor nanoparticles against photodegradation by a silica coating procedure. Chem Phys Lett 286(5–6):497–501
103. Kobayashi Y, Shimizu N, Misawa K, Takeda M et al (2008) Preparation of amine free silica-coated AgI nanoparticles with modified Stöber method. Surf Eng 24(4):248–252
104. Rogach AL, Nagesha D, Ostrander JW, Giersig M et al (2000) “Raisin bun”-type composite spheres of silica and semiconductor nanocrystals. Chem Mater 12(9):2676–2685
105. Zhu MQ, Han JJ, Li ADQ (2007) CdSe/CdS/SiO_2 core/shell/shell nanoparticles. J Nanosci Nanotechnol 7(7):2343–2348
106. Zhang SC, Li XG (2004) Synthesis and characterization of $CaCO_3$@SiO_2 core-shell nanoparticles. Powder Technol 141(1–2):75–79
107. Wang D, Salaueiriño-Maceira V, Liz-Marzán LM, Caruso F (2002) Gold-silica inverse opals by colloidal crystal templating. Adv Mater 14(12):908–912
108. Liz-Marzán LM, Giersig M, Mulvaney P (1996) Synthesis of nanosized gold-silica core-shell particles. Langmuir 12(18):4329–4335
109. Kückelhaus S, Reis SC, Carneiro MF, Tedesco AC et al (2004) In vivo investigation of cobalt ferrite-based magnetic fluid and magnetoliposomes using morphological tests. J Magn Magn Mater 272:2402–2403
110. Baldi G, Bonacchi D, Innocenti C, Lorenzi G et al (2007) Cobalt ferrite nanoparticles: the control of the particle size and surface state and their effects on magnetic properties. J Magn Magn Mater 311(1):10–16
111. Tartaj P, del Puerto Morales M, Veintemillas-Verdaguer S, González-Carreño T et al (2003) The preparation of magnetic nanoparticles for applications in biomedicine. J Phys D Appl Phys 36(13):R182
112. Lin YS, Haynes CL (2009) Synthesis and characterization of biocompatible and size-tunable multifunctional porous silica nanoparticles. Chem Mater 21(17):3979–3986
113. Cannas C, Musinu A, Ardu A, Orrù F et al (2010) $CoFe_2O_4$ and $CoFe_2O_4$/SiO_2 core/shell nanoparticles: magnetic and spectroscopic study. Chem Mater 22(11):3353–3361
114. Hu YX, Ge JP, Sun YG, Zhang TR et al (2007) A self-templated approach to TiO_2 microcapsules. Nano Lett 7(6):1832–1836
115. Ge JP, Hu YX, Biasini M, Beyermann WP et al (2007) Superparamagnetic magnetite colloidal nanocrystal clusters. Angew Chem Int Ed 46(23):4342–4345
116. Ge JP, Huynh T, Hu YX, Yin YD (2008) Hierarchical magnetite/silica nanoassemblies as magnetically recoverable catalyst-supports. Nano Lett 8(3):931–934
117. Obrovac MN, Krause LJ (2007) Reversible cycling of crystalline silicon powder. J Electrochem Soc 154(2):A103–A108

118. Maranchi JP, Hepp AF, Kumta PN (2003) High capacity, reversible silicon thin-film anodes for lithium-ion batteries. Electrochem Solid-State Lett 6(9):A198–A201
119. Limthongkul P, Jiang YI, Dudney NJ, Chiang YM (2003) Electrochemically-driven solid-state amorphization in lithium-silicon alloys and implications for lithium storage. Acta Mater 51(4):1103–1113
120. Chan CK, Peng HL, Liu G, Mcllwrath K et al (2008) High-performance lithium battery anodes using silicon nanowires. Nat Nanotechnol 3(1):31–35
121. Cui LF, Ruffo R, Chan CK, Peng HL et al (2009) Crystalline-amorphous core-shell silicon nanowires for high capacity and high current battery electrodes. Nano Lett 9(1):491–495
122. Freeman RG, Hommer MB, Grabar KC, Jackson MA et al (1996) Ag-clad Au nanoparticles: novel aggregation, optical, and surface-enhanced Raman scattering properties. J Phys Chem 100(2):718–724
123. Toshima N, Yonezawa T (1998) Bimetallic nanoparticles-novel materials for chemical and physical application. New J Chem 22(11):1179–1201
124. Tomas JM, Johnson BFG, Raja R, Sankar G et al (2003) High-performance nanocatalysts for single-step hydrogenations. Acc Chem Res 36(1):20–30
125. Scott RWJ, Wilson OM, Crooks RM (2005) Synthesis, characterization, and application of dendrimer-encapsulated nanoparticles. J Phys Chem B 109(2):692–704
126. Link S, Wang ZL, El-Sayed MA (1999) Alloy formation of gold-silver nanoparticles and the dependence of the plasmon absorption on their composition. J Phys Chem B 103(18):3529–3533
127. Hodak JH, Henglein A, Giersig M, Hartland GV (2000) Laser-induced inter-diffusion in AuAg core-shell nanoparticles. J Phys Chem B 104(49):11708–11718
128. Mallik K, Mandal M, Pradhan N, Pal T (2001) Seed mediated formation of bimetallic nanoparticles by UV irradiation: a photochemical approach for the preparation of “core-shell” type structures. Nano Lett 1(6):319–322
129. Mallin MP, Murphy CJ (2002) Solution-phase synthesis of sub-10 nm Au-Ag alloy nanoparticles. Nano Lett 2(11):1235–1237
130. Shibata T, Bunker BA, Zhang ZY, Meisel D et al (2002) Size-dependent spontaneous alloying of Au-Ag nanoparticles. J Am Chem Soc 124(40):11989–11996
131. Chen DH, Chen CJ (2002) Formation and characterization of Au-Ag bimetallic nanoparticles in water-in-oil microemulsions. J Mater Chem 12(5):1557–1562
132. Liu MZ, Guyot-Sionnest P (2004) Synthesis and optical characterization of Au/Ag core/shell nanorods. J Phys Chem B 108(19):5882–5888
133. Shankar SS, Rai A, Ahmad A, Sastry M (2004) Rapid synthesis of Au, Ag, and bimetallic Au core-Ag shell nanoparticles using Neem (Azadirachta indica) leaf broth. J Colloid Interf Sci 275(2):496–502
134. Hang CC, Yang Z, Chang HT (2004) Synthesis of dumbbell-shaped Au-Ag core-shell nanorods by seed-mediated growth under alkaline conditions. Langmuir 20(15):6089–6092
135. Song JH, Kim FK, Kim D, Yang PD (2005) Crystal overgrowth on gold nanorods: tuning the shape, facet, aspect ratio, and composition of the nanorods. Chem Eur J 11(3):910–916
136. Liu FK, Huang PW, Chang YC, Ko FH et al (2005) Combining optical lithography with rapid microwave heating for the selective growth of Au/Ag bimetallic core/shell structures on patterned silicon wafers. Langmuir 21(6):2519–2525
137. Xu SP, Zhao B, Xu WQ, Fan YG (2005) Preparation of Au-Ag coreshell nanoparticles and application of bimetallic sandwich in surface-enhanced Raman scattering (SERS). Colloids Surf A: Physicochem Eng Aspects 257–258:313–317
138. Wilson OM, Scott RWJ, Garcia-Martinez JC, Crooks RM (2005) Synthesis, characterization, and structure-selective extraction of 1-3 nm diameter AuAg dendrimer-encapsulated bimetallic nanoparticles. J Am Chem Soc 127(3):1015–1024

139. Pedersen DB, Wang SL, Duncan EJS, Liang SH (2007) Adsorbate-induced diffusion of Ag and Au atoms out of the cores of Ag@Au, Au@Ag, and Ag@AgI core-shell nanoparticles. J Phys Chem C 111(37):13665–13672
140. Rai A, Chaudhary M, Ahmad A, Bhargava S et al (2007) Synthesis of triangular Au core-Ag shell nanoparticles. Mater Res Bull 42(7):1212–1220
141. Tusji M, Miyamae N, Lim S, Kimura K (2006) Crystal structures and growth mechanisms of Au@Ag core-shell nanoparticles prepared by the microwave-polyol method. Cryst Growth Des 6(8):1801–1807
142. Tsuji M, Matsuo R, Jiang P, Miyamae N (2008) Shape-dependent evolution of Au@Ag core-shell nanocrystals by PVP-assisted *N,N*-dimethylformamide reduction. Cryst Growth Des 8(7):2528–2536
143. Yin YD, Rioux RM, Erdonmez CK, Hughes S et al (2004) Formation of hollow nanocrystals through the nanoscale Kirkendall effect. Science 304(5671):711–714
144. Sun YG, Xia YN (2002) Shape-controlled synthesis of gold and silver nanoparticles. Science 298(5601):2176–2179
145. Wang Y, Cai L, Xia Y (2005) Monodisperse spherical colloids of Pb and their use as chemical templates to produce hollow particles. Adv Mater 17(4):473–477
146. Liang HP, Zhang HM, Hu JS, Guo YG et al (2004) Pt hollow nanospheres: facile synthesis and enhanced electrocatalysts. Angew Chem Int Ed 116(12):1566–1569
147. Lou XW, Wang Y, Yuan C, Lee JY et al (2006) Template-free synthesis of SnO_2 hollow nanostructure with high lithium storage capacity. Adv Mater 18(17):2325–2329
148. Zeng HC (2006) Synthetic architecture of interior space for inorganic nanostructure. J Mater Chem 16(7):649–662
149. Caruso F, Caruso RA, Möhwald H (1998) Nanoengineering of inorganic and hybrid hollow spheres by colloidal templating. Science 282(5391):1111–1114
150. Yang ZZ, Niu ZW, Lu YF, Hu ZB et al (2003) Templated synthesis of inorganic hollow spheres with a tunable cavity size onto core-shell gel particles. Angew Chem Int Ed 42(17):1943–1945
151. Chen M, Wu L, Zhou S, You B (2006) A method for the fabrication of monodisperse hollow silica spheres. Adv Mater 18(6):801–806
152. Lou XW, Yuan CL, Archer LA (2007) Shell-by-shell synthesis of tin oxide hollow colloids with nanoarchitectured walls: cavity size tuning and functionalization. Small 3(2):261–265
153. Lou XW, Yuan C, Rhoades E, Zhang Q et al (2006) Encapsulation and Ostwald ripening of Au and Au-Cl complex nanostructures in silica shells. Adv Funct Mater 16(13):1679–1684
154. Kim SW, Kim M, Lee WY, Hyeon T (2002) Fabrication of hollow palladium spheres and their successful application to the recyclable heterogeneous catalyst for Suzuki coupling reactions. J Am Chem Soc 124(26):7642–7643
155. Dhas NA, Suslick KS (2005) Sonochemical preparation of hollow nanospheres and hollow nanocrystals. J Am Chem Soc 127(8):2368–2369
156. Zhou J, Liu J, Yang R, Lao CS et al (2006) SiC-shell nanostructures fabricated by replicating ZnO nano-objects: a technique for producing hollow nanostructures of desired shape. Small 2(11):1344–1347
157. Kamata K, Lu Y, Xia YN (2003) Synthesis and characterization of monodispersed core-shell spherical colloids with movable cores. J Am Chem Soc 125(9):2384–2385
158. Zhu YF, Kockrick E, Ikoma T, Hanagata N (2009) An efficient route to rattle-type $Fe_3O_4@SiO_2$ hollow mesoporous spheres using colloidal carbon spheres templates. Chem Mater 21(12):2547–2553
159. Zhou JB, Tang C, Cheng B, Yu JG et al (2012) Rattle-type carbon-alumina core-shell spheres: synthesis and application for adsorption of organic dyes. ACS Appl Mater Interfaces 4(4):2174–2179
160. Yu JG, Yu XX (2008) Hydrothermal synthesis and photocatalytic activity of zinc oxide hollow spheres. Environ Sci Technol 42(13):4902–4907

161. Sevilla M, Fuertes AB (2009) Chemical and structural properties of carbonaceous products obtained by hydrothermal carbonization of saccharides. Chem Eur J 15(16):4195–4203
162. Wang YQ, Nikitin K, McComb DW (2008) Fabrication of Au-Cu_2O core-shell nanocube heterostructures. Chem Phys Lett 456(4–6):202–205
163. Wagner JB, Sköld N, Wallenberg LR, Samuelson L (2010) Growth and segregation of Ga-As-$Al_xIn_{1-x}P$ core-shell nanowires. J Cryst Growth 312(10):1755–1760
164. Garcia-Gutierrez D, Gutierrez-Wing C, Miki-Yoshida M, Jose-Yacaman M (2004) HAADF study of Au-Pt core-shell bimetallic nanoparticles. Appl Phys Mater Sci Process 79(3):481–487
165. Ren F, Jiang CZ, Wang YH, Wang QQ et al (2006) The problem of core/shell nanoclusters formation during ion implantation. Nucl Instrum Methods Phys Res B 245(2):427–430
166. Wang JX, Inada H, Wu LJ, Zhu YM et al (2009) Oxygen reduction on well-defined core-shell nanocatalysts: particle size, facet, and Pt shell thickness effects. J Am Chem Soc 131(47):17298–17302
167. Tak Y, Hong SJ, Lee JS, Yong K (2009) Fabrication of ZnO/CdS core/shell nanowire arrays for efficient solar energy conversion. J Mater Chem 19(33):5945–5951
168. Strasser P, Koh S, Anniyev T, Greeley J et al (2010) Lattice-strain control of the activity in dealloyed core-shell fuel cell catalysts. Nat Chem 2(6):454–460
169. Wu Y, Jiang P, Jiang M, Wang TW et al (2009) The shape evolution of gold seeds and gold@silver core-shell nanostructures. Nanotechnology 20(30):305602
170. Serpell CJ, Cookson J, Ozkaya D, Beer PD (2011) Core@shell bimetallic nanoparticle synthesis via anion coordination. Nat Chem 3(6):478–482
171. Li ZY, Yuan J, Chen Y, Palmer RE et al (2005) Direct imaging of core-shell structure in silver-gold bimetallic nanoparticles. Appl Phys Lett 87(24):243103
172. Habas SE, Lee H, Radmilovic V, Somorjai GA et al (2007) Shaping binary metal nanocrystals through epitaxial seeded growth. Nat Mater 6(9):692–697
173. Sanchez SI, Small MW, Zuo JM, Nuzzo RG (2009) Structure characterization of Pt-Pd core-shell nanoclusters at atomic resolution. J Am Chem Soc 131(24):8683–8689
174. Lim B, Jiang MJ, Camargo PHC, Cho EC (2009) Pd-Pt bimetallic nanodendrites with high activity for oxygen reduction. Science 324(5932):1302–1305
175. Lin G, Heggen M, Rudi S, Strasser P (2012) Core-shell compositional fine structures of dealloyed Pt_xNi_{1-x} nanoparticles and their impact on oxygen reduction catalysis. Nano Lett 12(10):5423–5430
176. Kim K, Kim KL, Shin KS (2011) Coreduced Pt/Ag alloy nanoparticles: surface-enhanced raman scattering and electrocatalytic activity. J Phys Chem C 115(47):23374–23380
177. Greene LE, Law M, Yuhas BD, Yang PD (2007) ZnO-TiO_2 core-shell nanorod/P3HT solar cells. J Phys Chem C 111(50):18451–18456
178. Lin HM, Chen YL, Yang J, Liu YC et al (2003) Synthesis and characterization of core-shell CaP@GaN and GaN@GaP nanowires. Nano Lett 3(4):537–541
179. Law M, Greene LE, Radenovic A, Kuykendall T et al (2006) ZnO-Al_2O_3 and ZnO-TiO_2 core-shell nanowire dye-sensitized solar cells. J Phys Chem B 110(45):22652–22663
180. Lauhon LJ, Gudiksen MS, Wang DL, Lieber CM (2002) Epitaxial core-shell and core-multishell nanowire heterostructures. Nature 420(6911):57–61
181. Algra RE, Hocevar M, Verheijen MA, Zardo I et al (2011) Crystal structure transfer in core/shell nanowires. Nano Lett 11(4):1690–1694
182. Kim H, Achermann M, Balet LP, Hollingsworth JA et al (2005) Synthesis and characterization of Co/CdSe core/shell nanocomposites: bifunctional magnetic-optical nanocrystals. J Am Chem Soc 127(2):544–546
183. Lambert K, Geyter BD, Moreels I, Hens Z (2009) PbTe|CdTe core|shell particles by cation exchange, a HR-TEM study. Chem Mater 21(5):778–780
184. Kong XY, Ding Y, Wang ZL (2004) Metal-semiconductor Zn-ZnO core-shell nanobelts and nanotubes. J Phys Chem B 108(2):570–574

185. Pietryga JM, Werder DJ, Williams DJ, Casson JL (2008) Utilizing the lability of lead selenide to produce heterostructured nanocrystals with bright, stable infrared emission. J Am Chem Soc 130(14):4879–4885
186. Koike K, Honden T, Makabe I, Yan FP et al (2003) PbTe/CdTe single quantum wells grown on GaAs (100) substrates by molecular beam epitaxy. J Cryst Growth 257(1–2):212–217
187. Huang MH, Mao S, Feick H, Yan HQ et al (2001) Room-temperature ultraviolet nanowire nanolasers. Science 292(5523):1897
188. Arnold MS, Avouris P, Pan ZW, Wang ZL (2003) Field-effect transistors based on single semiconducting oxide nanobelts. J Phys Chem B 107(3):659
189. Comini E, Faglia G, Sberveglieri G, Pan ZW et al (2002) Stable and highly sensitive gas sensors based on semiconducting oxide nanobelts. Appl Phys Lett 81(10):1869
190. Hughes WL, Wang ZL (2003) Nanobelts as nanocantilevers. Appl Phys Lett 82(17):2886
191. Bai XD, Gao PX, Wang ZL, Wang EG (2003) Dual-mode mechanical resonance of individual ZnO nanobelts. Appl Phys Lett 82(26):4806
192. Pan ZW, Dai ZR, Wang ZL (2001) Nanobelts of semiconducting oxides. Science 291(5510):1947
193. Gallaso F (1970) Structure and properties of inorganic solids. Pergamon, Oxford
194. Nguyen VL, Ohtaki M, Matsubara T, Cao MT et al (2012) New experimental evidences of Pt-Pd bimetallic nanoparticles with core-shell configuration and highly fine-ordered nanostructures by high-resolution electron transmission microscopy. J Phys Chem C 116(22):12265–12274
195. Schlötzer-Schrehardt U, Körtje KH, Erb C (2001) Energy-filtering transmission electron microscopy (EFTEM) in the elemental analysis of pseudoexfoliative material. Curr Eye Res 22(2):154–162
196. Leapman RD, Kocsis E, Zhang G, Talbot TL et al (2004) Three-dimensional distributions of elements in biological samples by energy-filtered electron tomography. Ultramicroscopy 100(1–2):115–125
197. Wang YQ, Duan XF, Cao LM, Wang WK (2002) One-dimensional growth mechanism of amorphous boron nanowires. Chem Phys Lett 359(3–4):273–277
198. Wang YQ, Duan XF, Cao LM, Li G et al (2002) Application of energy-filtering transmission electron microscopy to characterize amorphous boron nanowires. J Cryst Growth 244(1):123–128
199. Tambe MJ, Lim SK, Smith MJ, Allard LF et al (2008) Realization of defect-free epitaxial core-shell GaAs/AlGaAs nanowire heterostructures. Appl Phys Lett 93(15):151917
200. Morales AM, Lieber CM (1998) A laser ablation method for the synthesis of crystalline semiconductor nanowires. Science 279(5348):208–211
201. Zhang YF, Tang YH, Wang N, Lee CS (2000) Germanium nanowires sheathed with an oxide layer. Phys Rev B 61(7):4518–4521
202. Cao LM, Zhang Z, Sun LL, Gao CX et al (2001) Well-aligned boron nanowire arrays. Adv Mater 13(22):1701–1704
203. Qian F, Li Y, Gradečak S, Wang DL et al (2004) Gallium nitride-based nanowire radial heterostructures. Nano Lett 4(10):1975–1979
204. Hiramatsu K, Nishiyama K, Motogaito A, Miyake H et al (1999) Recent progress in selective area growth and epitaxial lateral overgrowth of III-nitrides: effects of reactor pressure in MOVPE growth. Appl Mater Sci 176(1):535–543
205. Gerthsen D, Hahn E, Neubauer B, Potin V et al (2003) Indium distribution in epitaxially grown InGaN layers analyzed by transmission electron microscopy. Phys Status Solidi C 0(6):1668–1683